Scenario set-up and forcing data for impact model evaluation and impact attribution within the third round of the Inter-Sectoral Model Intercomparison Project (ISIMIP3a)

Katja Frieler[1], Jan Volkholz[1], Stefan Lange[1], Jacob Schewe[1], Matthias Mengel[1], María del Rocío Rivas López[1], Christian Otto[1], Christopher P.O. Reyer[1], Dirk Nikolaus Karger[2], Johanna T. Malle[2], Simon Treu[1], Christoph Menz[1], Julia L. Blanchard[3], Cheryl S. Harrison[4], Colleen M. Petrik[5], Tyler D. Eddy[6], Kelly Ortega-Cisneros[7], Camilla Novaglio[3], Yannick Rousseau[3], Reg A. Watson[3], Charles Stock[8], Xiao Liu[9], Ryan Heneghan[10], Derek Tittensor[11], Olivier Maury[12], Matthias Büchner[1], Thomas Vogt[1], Tingting Wang[13], Fubao Sun[13], Inga J. Sauer[1,14], Johannes Koch[1], Inne Vanderkelen[15, 16, 17], Jonas Jägermeyr[1,18, 19], Christoph Müller[1], Jochen Klar[1], Iliusi D. Vega del Valle[1], Gitta Lasslop[20], Sarah Chadburn[21], Eleanor Burke[22], Angela Gallego-Sala[23], Noah Smith[21], Jinfeng Chang[24], Stijn Hantson[25], Chantelle Burton[22], Anne Gädeke[1], Fang Li[26], Simon N. Gosling[27], Hannes Müller Schmied[20, 28], Fred Hattermann[1], Jida Wang[29], Fangfang Yao[30], Thomas Hickler[20], Rafael Marcé[31,32], Don Pierson[33], Wim Thiery[15], Daniel Mercado-Bettín[31], Matthew Forrest[20], Michel Bechtold[34]

Affiliations:
[1]Potsdam Institute for Climate Impact Research, 14473 Potsdam, Germany
[2]Swiss Federal Research Institute WSL, Zürcherstrasse 111, 8903 Birmensdorf, Switzerland
[3]Institute for Marine and Antarctic Studies, University of Tasmania, Hobart, Tasmania, Australia
[4]Department of Ocean and Coastal Science and Center for Computation and Technology, Louisiana State University, Baton Rouge, Louisiana, USA
[5]Scripps Institution of Oceanography, University of California San Diego, CA, USA
[6]Centre for Fisheries Ecosystems Research, Fisheries & Marine Institute, Memorial University, St. John's, NL, Canada
[7]Department of Biological Sciences, University of Cape Town, Rondebosch, Cape Town, 7701, South Africa
[8]NOAA/OAR/Geophysical Fluid Dynamics Laboratory, Princeton, NJ, United States
[9]SAIC@NOAA/NWS/NCEP Environmental Modeling Center, 5830 University Research Court, College Park, MD 20740
[10]School of Mathematical Sciences, Queensland University of Technology, Brisbane, QLD, Australia
[11]Department of Biology, Dalhousie University, Halifax, Nova Scotia, Canada, B3H 4R2
[12]Institute for Research for Development, UMR 248 MARBEC, France.
[13]Key Laboratory of Water Cycle and Related Land Surface Processes, Institute of Geographic Sciences and Natural Resources Research, Chinese Academy of Sciences, Beijing 100101, China
[14]Institute for Environmental Decisions, ETH Zurich, Zurich, Switzerland
[15]Vrije Universiteit Brussel, Department of Hydrology and Hydraulic Engineering, Brussels, Belgium
[16]Wyss Academy for Nature, University of Bern, Bern, Switzerland
[17]Climate and Environmental Physics and Oeschger Center for Climate Change Research, University of Bern, Bern, Switzerland
[18]NASA Goddard Institute for Space Studies, New York, NY 10025, USA
[19]Columbia University, Climate School, New York, NY 10025, USA

[20]Senckenberg Leibniz Biodiversity and Climate Research Centre (SBiK-F), Frankfurt am Main, Germany.

[21]Department of Mathematics, University of Exeter, Exeter UK

50 [22]Met Office Hadley Centre, Fitzroy Road, Exeter, UK

[23]Geography Department, University of Exeter, Exeter, UK

[24]College of Environmental and Resource Sciences, Zhejiang University, Hangzhou, China

[25]Faculty of Natural Sciences, Universidad del Rosario, Bogotá, Colombia

[26]International Center for Climate and Environment Sciences, Institute of Atmospheric Physics, Chinese

55 Academy of Sciences, Beijng, China

[27]School of Geography, University of Nottingham, Nottingham, UK

[28]Institute of Physical Geography, Goethe University Frankfurt, Frankfurt am Main, Germany

[29]Department of Geography and Geospatial Sciences, Kansas State University, Manhattan, Kansas, USA

60 [30]Environmental Resilience Institute, University of Virginia, Charlottesville, Virginia 22903, USA

[31]Catalan Institute for Water Research (ICRA), 17003 Girona, Spain

[32]Universitat de Girona, Girona, Spain

[33]Uppsala University, Norbyvägen 18 D, 752 36 Uppsala, Sweden

[34]KU Leuven, Department of Earth and Environmental Sciences, Leuven, Belgium

Correspondence to: Katja Frieler (katja.frieler@pik-potsdam.de)

Abstract. This paper describes the rationale and the protocol of the first component of the third

simulation round of the Inter-Sectoral Impact Model Intercomparison Project (ISIMIP3a,

70 www.isimip.org) and the associated set of climate-related and direct human forcing data (CRF and

DHF, respectively). The observation-based climate-related forcings for the first time include high-

resolution observational climate forcings derived by orographic downscaling, monthly to hourly coastal

water levels, and wind fields associated with historical tropical cyclones. The DHFs include land use

patterns, population densities, information about water and agricultural management, and fishing

75 intensities. The ISIMIP3a impact model simulations driven by these observation-based climate-related

and direct human forcings are designed to test to what degree the impact models can explain observed

changes in natural and human systems. In a second set of ISIMIP3a experiments the participating

impact models are forced by the same DHFs but a counterfactual set of atmospheric forcings and

coastal water levels where observed trends have been removed. These experiments are designed to

80 allow for the attribution of observed changes in natural, human and managed systems to climate

change, rising CH_4 and CO_2 concentrations, and sea level rise according to the definition of the Working

Group II contribution to the IPCC AR6.

1 Introduction

85 The Inter-Sectoral Impact Model Intercomparison Project ISIMIP (www.isimip.org) provides a common

scenario framework for cross-sectorally consistent climate impact simulations currently covering the

following sectors: agriculture (global; in cooperation with AgMIP's Global Gridded Crop Model

Intercomparison Project (GGCMI)), water (global and regional), lakes (global and regional), biomes

(global), forest (regional), fisheries and marine ecosystems (global and regional), terrestrial biodiversity

90 (global), fire (global), permafrost (global), peat (global), coastal systems (global), energy (global), health

(temperature-related mortality; water-borne diseases; vector-borne diseases; and food security and

nutrition) (global and local), and labour productivity (global and local). The impact model simulations are made freely available, allowing for all types of follow-up analysis. The consistent design of the simulations does allow for the comparison of climate impact simulations within each sector. However, it also enables the bottom-up integration of impacts across sectors. Thus, it provides a unique basis for the estimation of the effects of climate change on, e.g., the economy, displacement and migration, health, or water quality resolving the mechanisms along different impact channels and fully exploiting the process-understanding represented in the biophysical impact models.

ISIMIP is organised in individual modelling rounds allowing to track the progress in impact model development particularly based on the historical evaluation runs within the 'a' part of the simulation rounds. Compared to ISIMIP2a, ISIMIP3a for the first time includes i) an 'attribution' scenario set-up allowing for the attribution of observed changes in natural, human, or managed systems to changes in climate-related systems including climate change itself, changes in atmospheric CO_2 and CH_4 concentration and sea level changes (see sections **2.2** for the associated concept and scenario design and **3.1** and **3.3** for the required counterfactual climate and sea level forcing data, respectively) and ii) sensitivity experiments using high resolution historical climate forcing data (see section **3.1**) to quantify associated improvements of impact simulations. The historical set of observation-based direct human forcings that have been updated compared to previous ISIMIP simulation rounds (see **Table 1**).

The development of the ISIMIP3 protocol was coordinated by the ISIMIP-Cross-Sectoral Science Team (CSST) at the Potsdam Institute for Climate Impact Research (PIK) and involved the sectoral coordinators, participating modelling teams, and the Scientific Advisory Board. The process was initiated by a proposal for the main research questions to be addressed and an associated scenario set-up accounting for suggestions collected in a stakeholder engagement process (Lejeune et al., 2018). Following ISIMIP's mission and implementation document (ISIMIP Coordination Team, Sectoral Coordinators, Scientific Advisory Board, 2018), the basic proposal was approved by the ISIMIP strategy group at the cross-sectoral ISIMIP workshop in Potsdam, September 2018 (Outcomes of the ISIMIP Strategy Group Meeting, 2018). Thereby the CSST and the sectoral coordinators were tasked to translate the decisions into a cross-sectorally consistent simulation protocol and to generate, pre-process or collect the required climate-related and direct human forcing data. This paper presents the results of this process and the motivation and reasoning behind the individual steps for ISIMIP3a, while another paper provides the same information for ISIMIP3b dedicated to future impact projections based on climate model simulations (Frieler et al., submitted 2023). It provides the point of reference for modelling teams interested in participating in ISIMIP3a but also for users of the impact simulation data, which become freely accessible according to the ISIMIP terms of use (ISIMIP terms of use, 2022). The paper is accompanied by a simulation protocol (ISIMIP3a simulation protocol, 2023) providing all technical details such as file and variable naming conventions and sector-specific lists of output variables to be reported by the participating modelling teams. The ISIMIP3 simulation round was officially started on 21st February 2020[1] with the release of the associated protocol. Since then, the

---

[1] announced via email to the ISIMIP mailing list from 21st February 2020

protocol has already received some updates through the addition of output variables, correction of errors, and inclusion of new sectors. This paper refers to the protocol version of 14th January 2023. However, the protocol may still receive updates similar to the ones mentioned above. Impact modellers interested in contributing to ISIMIP should therefore refer to ISIMIP3a simulation protocol, 2023 for the

135 most up to date reference for planned impact model simulations. It includes a unique version identifier on its front page for traceability.

In the second round of ISIMIP the observation-based model evaluation part (ISIMIP2a) was temporally separate from the climate model-based second part (ISIMIP2b, Frieler et al., 2017). This has led to

140 inconsistencies in the models and model versions contributing to ISIMIP2a and ISIMIP2b. Also, not all models providing future projections within ISIMIP2b also provided model evaluation runs for ISIMIP2a. To avoid this problem and ensure that each model's set of future projections is accompanied by associated historical simulations allowing for model evaluation, in the third simulation round, the ISMIP3a and ISIMIP3b protocols were released together and participating in ISIMIP3 means

145 contributing to ISIMIP3a and ISIMIP3b using the same impact model versions.

In the following, we describe the rationale behind the individual scenario set-ups (section **2**). Detailed description of the climate-related forcing data sets (see CRF section of **Table 1**) are provided in the third section: atmospheric climate data in section **3.1**; tropical cyclone data in section **3.2**; coastal water

150 levels in section **3.3**, and the ocean data in section **3.4**. Section 4 presents the ISIMIP3a direct human forcing data sets (see DHF section of **Table 1**), comprising population data (section **4.1**), gross domestic product (section **4.2**), land use and irrigation patterns (section **4.3**), fertiliser inputs (section **4.4**), land transformations (section **4.5**), nitrogen deposition (section **4.6**), crop calendar (section **4.7**), dams and reservoirs (section **4.8**), fishing intensities (section **4.9**), regional forest management (section **4.10**),

155 and desalination (section **4.11**).

2 Experiments and underlying rationale

All ISIMIP experiments are described by specifying the underlying set of climate-related forcings and

160 direct human forcings. In the following the individual experiments are introduced by defining the combination of both types of forcing data sets, where the associated specifiers to be used in the file naming are indicated in brackets (CRF specifier + DHF specifier) in the subheadings naming the experiments. The different combinations of the default sets of ISIMIP3a CRFs ('obsclim', 'counterclim') and DHFs ('histsoc', '2015soc', '1901soc', '1850soc', 'nat') are sketched in **Figure 1** and described in

165 more detail below. Some of the forcing data sets are mandatory: i.e. if impact models account for the forcing, the specified dataset must be used; if an alternative input data set is used instead, the run cannot be considered an ISIMIP simulation. We also provide optional forcing data that could be used but are not mandatory in the above sense (see **Table 1** for the definition of the default forcing data sets). In addition, the protocol includes a set of sensitivity experiments that are described as deviations from

170 the default runs and labelled by the baseline CRF and DHF settings and a third specifier indicating the

deviation from this default setting. The ISIMIP3a sensitivity runs include experiments with high-resolution climate forcing ('30arcsec', '90arcsec', '300arcsec', or '1800arcsec'), fixed levels of atmospheric CO_2 concentrations ('1901co2'), a scenario assuming no water management ('nowatermgt'), simulations excluding the occurrence of wildfires ('nofire'), keeping irrigation patterns at 1901 levels ('1901irr'), and assuming fixed 1955 riverine inputs of freshwater and nutrients into the ocean ('1955-riverine-input') (see **Table 2**).
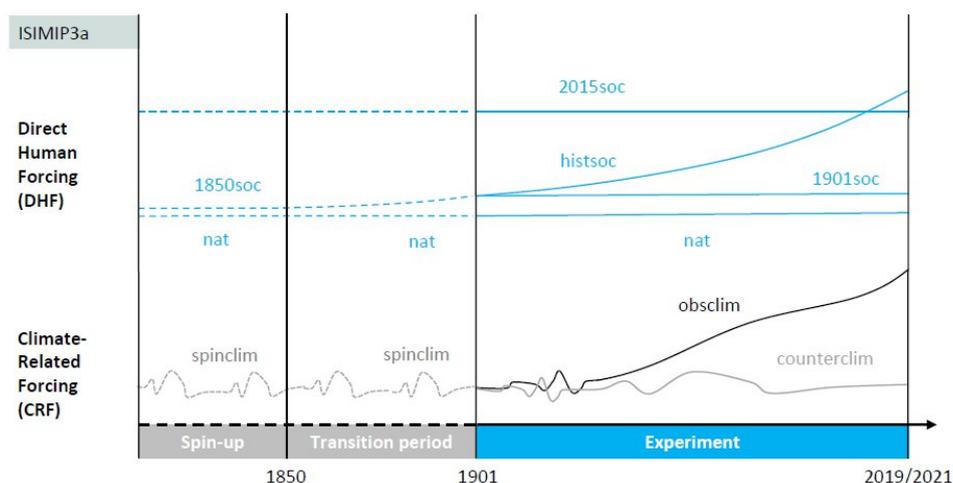
Figure 1: ISIMIP3a scenario design: Illustration of the default ISIMIP3a forcing data sets. Each experiment is defined by a combination of a CRF data set with a DHF data set. The considered combinations are listed in **Table 2** and **Table 4** and the underlying rationale is described in section **2.1** (evaluation runs based on 'obsclim' defined in **Table 1**) and section **2.2** (attribution runs based on 'counterclim' defined in **Table 3**). **Table 1** also lists all data sets defining the 'histsoc' DHF. Solid lines indicate the part of the experiments that should be reported while the dashed lines illustrate the different spin-up procedures for the models that require a spin-up. Note that the oceanic climate-related forcing for the *marine ecosystems and fisheries* sector is only available for 'obsclim' and the period 1961-2010, i.e. the actual experiments only start from the year 1961. The associated spin-up procedure and the simulations set-up for a transition period are not illustrated in the Figure but described below for the 'obsclim + histsoc, default', 'obsclim + nat, default', 'obsclim + histsoc, 60arcmin', and 'obsclim + nat, 60arcmin' experiments considered in this sector.

2.1 Model evaluation and sensitivity experiments based on observed CRFs ('obsclim')

In a first set of ISIMIP3a experiments, observed climate-related forcings ('obsclim', see CRF part of **Table 1**) are combined with different assumptions regarding direct human forcings ('histsoc', '2015soc', '1901soc', and 'nat').

Standard evaluation experiment using observed variations of direct human forcings (obsclim + histsoc; default). The first set of observation-based simulations is dedicated to impact model evaluation, i.e., to test our ability to reproduce and explain observed long-term changes or variations in impact indicators such as crop yields, river discharge, changes in natural vegetation carbon, vegetation

types, and peatland moisture conditions. To this end, we provide the climate-related ('obsclim'), direct human ('histsoc'), and static geographical forcings listed in **Table 1** and described in more detail in sections **3** and **4**.

205

For impact model simulations that require a spin-up to e.g. balance carbon stocks, 100 years of climate data ('spinclim') are provided that represent stable 1900 climate conditions. The spinclim data is equivalent to the first 100 years of the counterfactual climate data that are described in section **3.1**. If more than 100 years of spin-up are needed, the spinclim data can be repeated as often as needed. For

210 the spin-up, CO_2 concentrations and direct human forcing should be kept constant at 1850 levels. To get to the historical reporting period starting in 1901, modellers should simulate a transition period from 1850 to 1900 using spinclim climate data and the observed increase in CO_2 concentrations and historical changes in socioeconomic forcings (from 1850-1900).

215 The temporal coverage of the evaluation experiment is limited to 1961-2010 in the *marine ecosystems and fisheries* sector due to the availability of reanalysis-based oceanic forcing data (Liu et al., 2021). As spin-up + transition period for the 'obsclim + histsoc, default' experiments starting in 1961 the models should be run through six cycles of 1961-1980 '1955-riverine-input' CRFs (120 years, see **Table 1**) assuming reconstructed fishing efforts from 1861-1960 and constant 1861 levels before during 1841-

220 1860 (see **Table 1** and **Figure 3** in section **4.9**). If more years of spin-up are required, additional cycles of the 1961-1980 '1955-riverine-input' CRFs should be added, assuming constant 1861 fishing efforts.

225 **Table 1: Climate-related, direct human, and static geographic forcing data provided for the model evaluation and sensitivity experiments within ISIMIP3a.** The CRFs are grouped according to the definition of the default 'obsclim' CRF, the higher resolution '30arcsec', '90arcsec', '300arcsec', '1800arcsec' atmospheric CRF, the lower resolution '60arcmin' oceanic CRF, and the '1955-riverine-input' oceanic CRF for the sensitivity experiments. The listed set of DHFs defines the 'histsoc' set-up.

Forcing	Status	Source, description
Climate-Related Forcings ('obsclim')		
Atmospheric forcings		
Standard observation-based atmospheric climate forcing	mandatory	GSWP3-W5E5, 20CRv3-W5E5, 20CRv3-ERA5, 20CRv3, see section **3.1**
Local atmospheric climate forcing for lake locations	mandatory	Atmospheric data extracted from the data sets above for 72 lakes that have been identified within the *lake* sector as locations (grid cells of the ISIMIP 0.5° grid) where models can be calibrated based on observed temperature profiles and hypsometry (Golub et al., 2022).

Tropical cyclone tracks and windfields	mandatory	Tracks from IBTrACS database (period 1841-2021; Knapp et al., 2010). Windfields calculated by Holland model (Holland, 1980, 2008), see section **3.2**
Lightning	mandatory	Satellite-based (1995-2014) climatology of monthly flash rates (number of strokes km-2 d-1 on 0.5° grid (Cecil, 2006)
Oceanic forcings		
Standard observation-based oceanic forcing data	mandatory	GFDL MOM6/COBALTv2 simulations driven by reanalysis-based atmospheric forcing (Liu et al., 2021), see section **3.4**
Regional oceanic climate forcing for regional *marine ecosystems* and *fisheries* sector	mandatory	Extraction from data set above for 21 regional marine ecosystems. The extraction has been done for individual layers (ocean surface or bottom) and a subset of the variables that have been integrated along the ocean column (see Table 8).
Coastal water levels		
Coastal water levels	mandatory	Hourly coastal water levels with long-term trends for impact attribution, see section **3.3**
Atmospheric composition		
Atmospheric CO_2 concentration	mandatory	1850-2005: Meinshausen et al., 2011; 2006-2021: Global annual CO2 from NOAA Global Monthly Mean CO_2; Lan et al., 2023; Büchner and Reyer, 2022
Atmospheric CH_4 concentration	mandatory	1850-2014: Meinshausen et al., 2017; 2015-2021: Büchner and Reyer, 2022; Lan et al., 2023
Climate-Related Forcings for sensitivity experiments (30arcsec, 90arcsec, 300arcsec, 1800arcsec, 60arcmin, and 1955-riverine-input), identical to 'obsclim' except for:		
Atmospheric forcings (30arcsec, 90arcsec, 300arcsec, 1800arcsec)		
High resolution observation-based atmospheric forcing data	mandatory	see section **3.1** for a description of the CHELSA method applied to downscale the W5E5 observation-based atmospheric data to 30''. The data is then upscaled to 90" (~3 km), 300" (~10 km) and 1800'' = 0.5° (~60 km) to provide the forcings for additional sensitivity experiments.

Oceanic forcings (60arcmin)		
Low resolution observation-based oceanic forcing data	mandatory	GFDL MOM6/COBALTv2 simulations (1961 - 2010) driven by reanalysis-based atmospheric forcing (Liu et al., 2021) upscaled to 1°, see section **3.4**
Oceanic forcings (1955-riverine-input)		
Observation-based oceanic forcing data but assuming climatological 1951 to 1958 levels of riverine input	mandatory	GFDL MOM6/COBALTv2 simulations (1961 - 2010) driven by reanalysis-based atmospheric forcing (Liu et al., 2021), but fixed climatological 1951 to 1958 levels of freshwater input and input of nutrients and pollutants, see section **3.4**
Direct Human Forcing ('histsoc')		
Land use and irrigation	mandatory	HYDE-based irrigated and rainfed cropland downscaled to up to 15 crops, managed pasture and grassland, and urban areas, see section **4.3**
Wood harvest	optional	Historical annual country-level wood harvesting data based on the LUH2 v2h Harmonization Data Set (del Valle et al., 2022; Hurtt et al., 2011, 2020), see section **4.5**
Land transformation	mandatory	Historical annual land-use transformation data, based on the LUH v2h Harmonization Data Set (Hurtt et al., 2011, 2020), see section **4.5**
N-fertiliser inputs	mandatory	see section **4.4**
N-deposition	optional	Yang and Tian, 2020; Tian et al., 2018; see section **3.6**
Crop calendar	optional	Observation-based representation of recent average planting and maturity dates not accounting for changes over time (Jägermeyr et al., 2021a), see section **4.7**
Marine fishing effort	mandatory	Observation-based reconstruction of fishing effort spanning 1841-2010 (Rousseau et al., 2022 based on Rousseau et al., submitted 2023); see section **4.9** The climate-related forcing for the *marine ecosystems and fisheries* sector is only available for 1961-2010, but the spin-up procedure also requires fishing efforts for the earlier

		years (see description of the procedure for the 'obsclim + histsoc; default' scenario above).
Dams and reservoirs	optional	see section **4.8**
Water abstraction	optional	For modelling groups that do not have their own representation, we provide files containing the multi-model mean of domestic and industrial water withdrawal and consumption generated by the WaterGAP, PCR-GLOBWB, and H08 models (1850-2021). This data is based on ISIMIP2a 'varsoc' simulations for 1901-2005 and extended by RCP6.0 simulations from the Water Futures and Solutions project up to 2021 (Wada et al., 2016b). Years before 1901 have been filled with the value for year 1901.
Lake and reservoir surface area	optional	Total lake and reservoir area fractions (percentage of grid cell) calculated from the HydroLAKES v1.0 (Messager et al., 2016) and GRanDv1.3 databases (Lehner et al., 2011b) mapped to 0.5 degrees resolution. Areas increase with time because of the increasing number of reservoirs documented in GRanDv1.3. Reservoirs from 2017 onwards are kept constant. This data set differs from the lake surface areas provided as static geographic forcing (see below) which describe the surface area of one representative lake per grid cell and does not change over time.
Forest management	mandatory	Observed stem numbers, thinning type, planting numbers from and common management practices for 9 forest sites in Europe (Reyer et al., 2020b, 2023), see section **4.10**
Population data	mandatory	see section **4.1**
GDP data	mandatory	see section **4.2**
Static geographic forcing		
Lake volume at different depths	optional	The gridded data set describes the volume at different depths of one hypothetical lake representing the typical characteristics of all real lakes in the grid cell according to the GLOBathy (Khazaei et al., 2022; Messager et al., 2016) and HydroLAKES v1.0 (Khazaei et al., 2022; Messager et al., 2016) datasets (Golub et al., 2022). Each hypsographic

		curve consists of 11 data pairs. Level refers to the depth of the lake taking the lake bottom as the reference. Volume is the volume at the corresponding level.
Lake area at different depths	optional	The gridded data set describes the lake area at different depths of one hypothetical lake representing the typical characteristics of all real lakes in the grid cell according to the GLOBathy (Khazaei et al., 2022; Messager et al., 2016)and HydroLAKES (Khazaei et al., 2022; Messager et al., 2016) datasets (Golub et al., 2022). Each hypsographic curve consists of 11 data pairs. Level refers to the depth of the lake taking the lake bottom as the reference.
Lake elevation	optional	The gridded data set provides the elevation above sea level for the representative lakes described above. The information is derived from HydroLAKES v1.0 (Messager et al., 2016).
Maximum lake depth	optional	Gridded data set that provides the maximum depth for the representative lakes described above and derived from GLOBathy (Khazaei et al., 2022). We recommend using the area or volume hypsographic curves described above as inputs for your lake model. Use this file only if your lake model does not accept a full hypsographic curve as an input.
Lake depth	optional	Gridded data set that provides the mean depth for the representative lakes as calculated from GLOBathy and HydroLAKES v1.0 (Khazaei et al., 2022; Messager et al., 2016). We recommend using the area or volume hypsographic curves described above as inputs for your lake model. Use this file only if your lake model does not accept a full hypsographic curve as an input.
Lake volume	optional	Gridded data set of volume (km^3) for representative lakes described above as calculated from GLOBathy and HydroLAKES v1.0 (Khazaei et al., 2022; Messager et al., 2016). We recommend using the area or volume hypsographic curves described above as inputs for your lake model. Use this file only if your lake model does not accept a full hypsographic curve as an input.

Lake surface area	optional	Gridded data set of surface area for the representative lakes described above as calculated from GLOBathy and HydroLAKES v1.0 (Khazaei et al., 2022; Messager et al., 2016). As opposed to the "Lake and reservoir surface area" listed above under "Direct human forcing", this data set refers to one specific lake associated with each grid cell, and the corresponding surface area does not change over time. We recommend using the area or volume hypsographic curves described above as inputs for your lake model. Use this file only if your lake model does not accept a full hypsographic curve as an input.
HydroLAKES ID	optional	HydroLAKES reference to relate HydroLAKES and GLOBathy database fields to the representative lakes described above. This dataset contains IDs of the 41449 representative lakes used in ISIMIP, which are a subset of the about 1.4 million lakes contained in the HydroLAKES and GLOBathy database.
HydroLAKES IDs for big lakes	optional	This dataset is analogous to the one above, but only contains IDs of 93 large lakes. It can be used to produce global plots with conspicuous large lakes. To be used together with the file storing the big lakes mask.
Big lakes mask	optional	This dataset indicates the 0.5° grid cells actually occupied by each of the 93 large lakes, which can be larger than a single grid cell. It can be used to produce global plots with conspicuous large lakes. To be used together with the big lakes IDs in the dataset above.
Drainage direction map for river routing	optional	Includes for each grid cell a basin number, flow direction, and slope. Source: ISIMIPddm30 (Müller Schmied, 2022) based on DDM30 (Döll and Lehner, 2002)
Soil data	optional	Gridded soil characteristics have been generated within the Global Soil Wetness Project (GSWP3) (Dirmeyer et al., 2006; van den Hurk et al., 2016, GSWP3 documentation, 2023) and have already been provided within ISIMIP2a. Alternatively, we also provide maps of the dominant soil

		types (i.e., the type covering the largest fraction of the cell of the topmost soil layer) within each ISIMIP grid cell and the dominant soil types on the agricultural land within each ISIMIP grid cell. Both maps were derived from the Harmonized World Soil Database (HWSD Version 1.1, 2009) assuming that soil types are evenly distributed within the ISIMIP grid cells. We have used version 1.12 of the HWSD data at high resolution (30 arcsec). Information about the fraction of agricultural land within each ISIMIP 0.5°×0.5° grid cell was taken from MIRCA2000 (Portmann et al., 2010). If there is no soil information for an ISIMIP grid cell, e.g. due to differing land-sea-masks, the information from neighbouring cells is used. For further details please see GGCMI-HWSD (2023).
Land-sea mask	optional	We provide the binary land-sea mask of the W5E5 dataset. It is a conservative land mask where grid cells that in reality cover both land and ocean are counted as ocean. Thus, climate conditions over the land grid cells of this land-sea mask can be safely assumed to represent climate conditions over land rather than a mix of climate conditions over land and ocean. This refers to all climate datasets based on W5E5, i.e. GSWP3-W5E5 and 20CRv3-W5E5 of ISIMIP3a and the ISIMIP3b climate forcing that has been bias-adjusted using W5E5. The mask is also provided in a version without Antarctica. In addition, the generic land-sea mask from ISIMIP2b is provided to be used for global water simulations in ISIMIP3. It marks more grid cells as land than the main mask described above (Lange and Büchner, 2020).
Sea floor depth	optional	Grid cell level ocean depth in metres of GFDL-MOM6-COBALT2 data in 0.25 and 1° horizontal resolution
Binary country mask	optional	Binary country map on a 0.5° x 0.5° latitude-longitude grid
Fractional country mask	optional	Fractional country map on the ISIMIP 0.5° x 0.5° grid. This is the map that has been used to calculate the national data for ISIpedia (isipedia.org) and to e.g. prepare the national population and GDP data provided within ISIMIP3 (see sections **4.1** and **4.2**).

Large Marine Ecosystem masks	mandatory	Binary masks available at 0.25°, 0.5°, and 1° resolution (Sherman, 2017).
Regional Marine Ecosystem masks	optional	Binary masks describing the 21 ocean regions for the regional modelling activities in the fisheries and marine ecosystems available at 0.25° and 1° resolution. These masks have been used for the ocean forcing data extractions (see CRF part of this table).

Fixed 2015 direct human forcing (obsclim + 2015soc; default). To allow for the quantification of the effect of historical changes in direct human forcings, ISIMIP3a also contains an experiment where all direct human forcings are held constant at year 2015 levels. The difference between the evaluation run described above and this baseline simulation can be considered the impact of changes in direct human forcings. In addition, the simulated changes in models' output variables can be considered the 'pure effects of climate-related forcings', conditional on present-day socio-economic conditions. The experiment is also introduced because not all impact models can account for varying direct human forcings but rather assume fixed 'present day' conditions. All modelling teams are asked to do this experiment even if they are able to account for varying direct human forcings to generate one set of impact simulations that can be integrated across all participating models from different sectors or where all simulations from one sector can be compared. If a spin-up is required, it should be based on the 'spinclim' data as described above but fixed 2015 direct human forcings.

Impact of historical changes in direct human forcings - Fixed 1901 direct human forcing baseline (obsclim + 1901soc; default). Fixing direct human forcings at 1901 levels is an alternative approach to quantify i) the effects of direct human forcings when comparing these baseline simulations to the evaluation run and ii) the 'pure effect of observed change in climate-related systems', conditional on socio-economic conditions observed before the onset of this change. Because of the low levels of direct human forcings in 1901, this experiment is similar to the sector-specific 'nat' experiment that includes no direct human forcings whatsoever (see below). However, while the fully naturalised 'nat' run is suitable for the dynamic vegetation models from the *biomes* sector that simulate land cover by vegetation on their own, models in other sectors need land cover as an input. As this information is not available for pristine conditions, we introduce the 1901soc scenario such that models in the *water* sector can use land cover data approximately representative of 1901 conditions to describe a situation with minor human influences. If a spin-up is required, it should be based on the 'spinclim' data as described above but fixed 1901 direct human forcings.

Impact of direct human forcings - No direct human forcing baseline (obsclim + nat; default). To estimate the full effect of 2015 levels of DHF we also introduce a baseline 'nat' experiment that does not consider any DHFs but a natural state of the world. Then the difference to the 'obsclim + 2015soc, default' experiment can be considered the effect of 2015 levels of DHF. In addition, trends in the

260 'obsclim + nat; default' run only represent the impacts historical changes in the climate-related forcings would have had on an otherwise natural state of the world. While the '1901soc' condition may be similar to 'nat' conditions, trends in the 'obsclim + 1901soc; default' run may not only be induced by historical changes in the CRFs but could also represent lagged responses to changes in DHFs during the transition period. The 'nat' experiment can also be used to quantify the natural carbon sequestration

265 potential of natural vegetation without any management or land-use as an important counterfactual to assess the additionality of carbon sequestration measures. The 'nat' experiment is sector-specific for the *biomes, peat* and *marine ecosystems and fisheries* sectors. If a spin-up is required in the *biomes* and *peat* sector, it should be based on the 'spinclim' data as described above but assuming no direct human forcings. In the *marine ecosystems and fisheries* sector the spin-up should be based on the

270 '1955 riverine input' CRF as described for 'obsclim + histsoc, default' section but assuming no DHF, i.e. no fishing efforts.

High and low resolution sensitivity experiments (obsclim + histsoc; 30arcsec, 90arcsec, 300arcsec, 1800arcsec, and 60arcmin). To test whether high resolution atmospheric climate data

275 improve the climate impact model simulations, we also provide observational atmospheric forcing data at 30'' ('30arcsec'), 90'' ('90arcsec'), and 300'' ('300arcsec') resolution as well as atmospheric forcings at the original 1800'' resolution but derived from the 30'' (~1 km) data ('1800arcsec'). In addition, the oceanic data (original resolution of 0.25°) is upscaled to 1° to also test the sensitivity of the impact simulations to this modification ('60arcmin').

280 The 30'' atmospheric data (1979-2016) is derived from by a topographic downscaling of the observational W5E5 data (resolution of 0.5°) that particularly corrects for systematic effects induced by orographic details not represented in global reanalyses (CHELSA-W5E5, see section **3.1**). The data set comprises daily mean precipitation, daily mean surface downwelling shortwave radiation, daily mean near-surface air temperature, daily maximum near surface air temperature, daily minimum near

285 surface air temperature (see **Table 5**). We additionally provide simple approaches to downscale surface downwelling longwave radiation, near-surface relative humidity, air pressure and near-surface wind speed (see section **3.1**). Given the considerable storage capacities required by daily 1 km x 1 km data and constraints on data handling and download, we also aggregate the CHELSA-W5E5 data to 90'' (~3 km), 300'' (~10 km) and 1800'' = 0.5° (~60 km) to determine which resolution is required to improve the

290 impact model simulations compared to observed impact indicators. The evaluation of these historical sensitivity experiments will inform future downscaling activities for the GCM climate forcing data including future projections. The '1800arcsec' experiment is included as a reference, as the aggregated CHELSA-W5E5 data differ from the standard W5E5 data at the same resolution (see section **3.1**). So far the experiments have been added to the agriculture, lakes, global and regional water, regional

295 forests, terrestrial biodiversity, and labour protocol. However, they may be added to other sectors, too. The inclusion of the experiment is only constrained by the restricted set of variables included in CHELSA-W5E5. We do not provide spin-up data for the experiments. This means that models requiring a spin-up currently cannot perform the experiments. We will work on a solution on demand.

In contrast to the experiment testing the sensitivity of the impact simulations to a higher resolution of
300 the atmospheric CRFs, the associated sensitivity experiment for the *marine ecosystems and fisheries*
sector is not based on higher but on lower resolution oceanic data. While the default 'obsclim' oceanic
forcing data is derived by interpolating the observation-based historical ocean simulations from a tri-
polar 0.25° grid to a regular 0.25° grid (see section **3.4**), the CRFs for the sensitivity experiment are
derived by aggregating the default 'obsclim' data to a regular 1.0° grid ('60arcmin'). Evaluating the 1.0°
305 resolution is of interest because this is the resolution of the oceanic forcing data in ISIMIP3b. The low
resolution simulations could either start from the end of the simulations of the transition period of the
associated higher resolution runs ('obsclim + histsoc; default') or starting conditions could be newly
generated by following the 'spin-up + transition' procedure of 'obsclim + histsoc; default' experiment but
using the low-resolution '1955-riverine-input' CRF from the years 1961-1980.

310

Low resolution sensitivity experiment (obsclim + nat; 60arcmin). This sensitivity experiment for
the *marine ecosystems and fisheries* sector is analogous to the 'obsclim + nat; default' experiment
described further above, but using the lower-resolution oceanic CRF ('60arcmin'). The difference
between this experiment and the 'obsclim + histsoc; 60arcmin' sensitivity experiment can be considered
315 the effect of 2015 levels of DHF as estimated using lower-resolution CRF, and comparison with the
same difference in the default experiments then indicates how the estimate of this effect depends on
the resolution of the oceanic forcing. The simulations could either start from the end of the simulations
of the transition period of the associated higher resolution runs ('obsclim + nat; default') or starting
conditions could be newly generated by following the 'spin-up + transition' procedure of 'obsclim + nat,
320 default' experiment but using the low-resolution '1955-riverine-input' CRF from the years 1961-1980.

**CO_2 sensitivity experiments (obsclim + histsoc, obsclim + 2015soc, or obsclim + 1901soc;
1901co2).** To quantify the pure effect of the historical increase in atmospheric CO_2 concentrations on
vegetation leaf gas exchange and follow-on effects on carbon stocks, water use efficiency, vegetation
325 distribution etc., we introduced three sensitivity experiments where atmospheric CO_2 concentrations
are held constant at 1901 levels (= 296.13 ppm) in contrast to the default 'obsclim + histsoc', 'obsclim
+ 2015soc', or 'obsclim + 1901soc' experiments, respectively, where atmospheric CO_2 concentrations
are assumed to increase according to observations. The effect is known as CO_2 fertilisation through an
increase of the photosynthesis rate of plants and limited leaf transpiration (increase in water use
330 efficiency) enabling a more efficient uptake of carbon by the plants. The experiment is included into the
protocols of the *agriculture, terrestrial biodiversity, biomes, fire, lakes (global and local), permafrost,
peat and water (global and regional)* sector. A potentially required spin-up should be identical to the
spin-up for the associated default experiments using the transition period 1850-1900 to reach the 1901
CO_2 level.

335

Water management sensitivity experiment (obsclim + histsoc, obsclim + 2015soc; nowatermgt).
In this "no water management" experiment, models are run assuming no human water abstraction, no
dams or reservoirs, and no seawater desalination, while other direct human forcings such as land use

changes are considered according to 'histsoc' or '2015soc'. By comparison to the default experiments,
340   the simulations allow for a quantification of the pure effects of dedicated water management measures
on, e.g., discharge. The sensitivity experiment has been introduced into the *global and regional water*
sector protocols. If a spin-up is required, it should be done similar to the spin-up for the associated
default experiments but assuming "no water management".

345   **Irrigation sensitivity experiment (obsclim + histsoc, 1901irr).** In this "no irrigation expansion"
experiment, models are run assuming irrigation extent and irrigation water use efficiencies fixed at the
year 1901, while other direct human forcings such as land use changes and water management
categories are considered according to 'histsoc' or '2015soc'. By comparison to the default experiments,
the simulations allow for a quantification of the pure effects of historical irrigation expansion. The
350   sensitivity experiment has been introduced into the *global water and biome* sector protocols. If a spin-
up is required, it should be done similar to the spin-up for the associated default experiments but
assuming "no irrigation expansion". This experiment is designed such that its outcomes are comparable
to those of the Irrigation Impacts Model Intercomparison Project (IRRMIP;
https://hydr.vub.be/projects/irrmip), in which Earth System Models simulate irrigation influences on the
355   Earth system.

No-fire sensitivity experiment (obsclim + histsoc; nofire). In this 'nofire' experiment, fire is switched
off in the model simulations. In comparison to the default 'obsclim + histsoc' simulations, the historical
effects of fires on, e.g., carbon fluxes and vegetation distributions can be determined. The sensitivity
360   experiment has been introduced into the *fire, biomes, permafrost, and peat* protocols. The required
spin-up should be done similar to the spin-up for the associated default experiments but assuming no
fire activities.

Table 2: ISIMIP3a evaluation and sensitivity experiments

Experiment	Short description	Period: Historical 1901-2019
model evaluation histsoc 1st priority	**CRF:** Observed climate change, CO_2 and CH_4 levels, and coastal water levels	**obsclim**
	DHF: Varying direct human influences according to observations	**histsoc**
model evaluation	**CRF:** Observed climate change, CO_2 and CH_4 levels, and coastal water levels	**obsclim**

2015soc **1st priority**	**DHF:** Fixed 2015 levels of direct human forcing for the entire time period	**2015soc**
model evaluation 1901soc **2nd priority**	**CRF:** Observed climate change, CO_2 and CH_4 levels, and coastal water levels	**obsclim**
	DHF: Fixed 1901 levels of direct human forcing for the entire time period	**1901soc**
model evaluation nat **2nd priority**	**CRF:** Observed climate change, CO_2 and CH_4 levels, and coastal water levels	**obsclim**
	DHF: No direct human influences	**nat**
CO_2 sensitivity histsoc **2nd priority**	**CRF:** Observed climate change, CH_4 concentrations and coastal water levels, fixed CO_2 concentration at 1901 level	**obsclim** **Sensitivity experiment: 1901co2**
	DHF: Varying direct human influences according to observations	**histsoc**
CO_2 sensitivity 2015soc **2nd priority**	**CF:** Observed climate change, CH_4 concentrations and coastal water levels, fixed CO_2 concentration at 1901 level	**obsclim** **Sensitivity experiment: 1901co2**
	DHF: Fixed 2015 levels of direct human forcing for the entire time period	**2015soc**
CO_2 sensitivity 1901soc **2nd priority**	**CRF:** Observed climate change, CH_4 concentrations and coastal water levels, fixed CO_2 concentration at 1901 level	**obsclim** **Sensitivity experiment: 1901co2**
	DHF: Fixed 1901 levels of direct human forcing for the entire time period	**1901soc**

Water management sensitivity histsoc **2nd priority**	**CRF:** Observed climate change, coastal water levels, and CO_2 and CH_4 concentrations	**obsclim**
	DHF: No accounting for water management but representation of other direct human influences such as land use changes according to "histsoc"	**histsoc** **Sensitivity experiment: nowatermgt**
Water management sensitivity 2015soc **2nd priority**	**CRF:** Observed climate change, coastal water levels, and CO_2 and CH_4 concentrations	**obsclim**
	DHF: No accounting for water management but representation of other direct human influences such as land use patterns according to "2015soc"	**2015soc** **Sensitivity experiment: nowatermgt**
Irrigation sensitivity histsoc **2nd priority**	**CRF:** Observed climate change, coastal water levels, and CO_2 and CH_4 concentrations	**obsclim**
	DHF: Fixed year-1901 irrigation areas and water use efficiencies but representation of other direct human influences such as land use changes according to "histsoc"	**histsoc** **Sensitivity experiment: 1901irr**
No-fire sensitivity histsoc **1st priority**	**CRF:** Observed climate change, coastal water levels, CO_2 and CH_4 concentrations	**obsclim**
	DHF: Varying direct human influences according to observations	**histsoc** **Sensitivity experiment: nofire**
Riverine influx sensitivity histsoc **1st priority**	**CRF:** Observation-based oceanic forcing data, but with constant riverine nutrient and freshwater influx.	**obsclim** **Sensitivity experiment: 1955-riverine-input**
	DHF: Varying direct human influences according to observations	**histsoc**

Riverine influx sensitivity nat **1st priority**	**CRF:** Observation-based oceanic forcing data, but with constant riverine nutrient and freshwater influx.	**obsclim** **Sensitivity experiment: 1955-riverine-input**
	DHF: No direct human influences	**nat**
H i g h - r e s o l u t i o n sensitivity, 1km histsoc **2nd priority**	**CRF:** Observed high-resolution climate forcing (30''), coastal water levels, and CO_2 and CH_4 concentrations. For this experiment only 1979-2016 is covered	**obsclim** **Sensitivity experiment: 30arcsec**
	DHF: Varying direct human influences according to observations	**histsoc**
H i g h - r e s o l u t i o n sensitivity, 3km histsoc **2nd priority**	**CRF:** Observed high-resolution climate forcing (90''), coastal water levels, and CO_2 and CH_4 concentrations. For this experiment only 1979-2016 is covered	**obsclim** **Sensitivity experiment: 90arcsec**
	DHF: Varying direct human influences according to observations	**histsoc**
H i g h - r e s o l u t i o n sensitivity, 12km histsoc **2nd priority**	**CRF:** Observed high-resolution climate forcing (360''), coastal water levels, and CO_2 and CH_4 concentrations. For this experiment only 1979-2016 is covered	**obsclim** **Sensitivity experiment: 360arcsec**
	DHF: Varying direct human influences according to observations	**histsoc**
H i g h - r e s o l u t i o n sensitivity, 60km histsoc **2nd priority**	**CRF:** Observed climate forcings aggregated from high-resolution data, coastal water levels, CO_2 and CH_4 concentrations. For this experiment only 1979-2016 is covered	**obsclim** **Sensitivity experiment: 1800arcsec**
	DHF: Varying direct human influences according to observations	**histsoc**

Low-resolution sensitivity, 1° in the ocean histsoc **2nd priority**	**CRF:** Observation-based oceanic forcing data	**obsclim** **Sensitivity experiment: 60arcmin**
	DHF: Varying direct human influences according to observations	**histsoc**
Low-resolution sensitivity, 1° in the ocean nat **2nd priority**	**CRF:** Observation-based oceanic forcing data	**obsclim** **Sensitivity experiment: 60arcmin**
	DHF: No direct human influences	**nat**

365

2.2 Counterfactual baseline simulations for impact attribution ('counterclim')

The second set of impact model simulations within ISIMIP3a is dedicated to the attribution of historical changes in natural, managed, and human systems to long-term changes in climate-related systems,
370   i.e. the atmosphere, ocean and cryosphere as physical or chemical systems. In ISIMIP3a, we address attribution to changes in the climate-related systems itself, e.g., trends in atmospheric temperature and precipitation, coastal water levels, and atmospheric CO_2 concentrations. The provided counterfactual forcing data comprises daily atmospheric climate derived from the ISIMIP observational climate datasets (see section **3.1**); daily counterfactual coastal water levels derived from the ISIMIP historical
375   coastal water level dataset (see section **3.3**); and constant 1901 atmospheric CO_2 and CH_4 concentrations (see **Table 3**). So far, we do not address attribution to long-term changes in i) the ocean (e.g. temperature or ocean acidification changes), ii) the cryosphere (e.g. glacier mass loss), and iii) tropical cyclone characteristics (e.g. trends in associated heavy precipitation or wind speeds) other than the effects mediated through sea level rise. **Table 3** lists the climate-related forcings defining the
380   'counterclim' experiments. The 'counterclim' climate-related forcings are combined with the observed direct human forcing to facilitate the attribution experiments listed in **Table 4**.

Table 3: ISIMIP3a counterfactual climate-related forcings ('counterclim')

Forcing	Status	Source, description
Climate-related forcings (counterclim)		

Atmospheric forcings		
Counterfactual 'no-climate change' atmospheric climate forcing	mandatory	Detrended versions of the GSWP3-W5E5, 20CRv3-W5E5, 20CRv3-ERA5, 20CRv3 data sets derived by the Attrici method, see section **3.1**
Local atmospheric climate forcing for lake location	mandatory	Atmospheric data extracted from the data sets above for 72 lakes that have been identified within the *lake* sector as locations (grid cells of the ISIMIP 0.5° grid) where models can be calibrated based on observed temperature profiles and hypsometry (depth and area).
Tropical cyclone tracks and windfields	mandatory	We do not provide 'no climate change' TC tracks and windfields but the original tracks from the IBTrACS database (Knapp et al., 2010; period 1841-2021) windfields calculated by Holland model (Holland, 2008, 1980) should be used in combination with the counterfactual water levels to estimate the impacts of sea level rise on TC induced damages, losses or replacement, see section **3.2**
Lightning	mandatory	We do not provide 'no climate change' lightning data. Instead the original Flash Rate Monthly Climatology (Cecil, 2006) should be used in the 'counterclim' set-up.
Oceanic forcings		
Oceanic forcing data	-	We do not provide any counterfactual oceanic forcings, i.e. there is no 'no climate change' experiment proposed for the *marine ecosystems and fisheries* sector.
Atmospheric composition or fluxes		
Atmospheric CO_2 concentration	mandatory	1901 levels ([CO_2] = 296.13 ppm) of observed atmospheric CO_2 concentrations according to Meinshausen et al., 2011

Atmospheric CH_4 concentration	mandatory	1901 levels of atmospheric CH_4 concentrations ($[CH_4]$ = 928.80 ppb), according to Meinshausen et al., 2017

385   The attribution question "To what degree have observed changes in the climate-related systems contributed to observed changes in natural, human or managed systems?" could refer to individual events (e.g. to what extent has long-term climate change contributed to the observed extent of a specific river flood?) or long-term changes (e.g. to what extent have long-term climate change and increasing CO_2 fertilisation contributed to an observed change in crop yields?). In line with IPCC WG2 AR6, chapter

390   16 (O'Neill et al., 2022), an observed impact of climate change or any other change in a climate-related system is defined as the difference between the observed state of the human, natural or managed system and a counterfactual baseline that characterises the system's behaviour in the absence of changes in the climate-related systems. This counterfactual baseline may be stationary or vary in response to direct human influences such as changes in land use patterns, agricultural or water

395   management or population distribution and economic development affecting exposure and vulnerability to weather-related hazards.

   While the definition is quite straightforward, the number of studies addressing impact attribution based on this basic definition is still relatively small compared to the number of studies addressing climate

400   attribution, i.e. the question to what degree anthropogenic emissions of climate forcers, in particular greenhouse gases, have induced changes in the climate-related systems. While climate attribution is confronted by the challenge of separating the anthropogenically forced changes from the internal variability of the climate-related systems, climate impact attribution is about separating the impacts of observed changes in these climate-related systems from the effects of other direct (human) drivers of

405   changes in the considered natural, human or managed systems. Despite this difference, both climate and climate impact attribution share the feature that they rely on the comparison of the observed situation to a counterfactual situation that cannot be observed but simulated by either climate models (climate attribution) or climate impact models (impact attribution). In the case of impact attribution, that means simulations of the considered natural, human or managed system in the absence of climate

410   change, sea level rise, and changes in CO_2 concentrations. These simulations are now part of the ISIMIP3a protocol.

   Impact attribution relies on a high explanatory power of impact models for historical observations. As a first step, it has to be demonstrated that the processes represented in the impact model can explain the observed changes in the affected system, i.e. it has to be shown that the model forced by observed

415   changes in the climate-related systems ('obsclim') and accounting for the historical development of direct (human) forcings is able to reproduce the observed changes in the affected system (ISIMIP3a evaluation experiments, see section **2.1**). Thereby, models can either explicitly represent known changes in non-climate drivers such as known adjustments of fertiliser input or growing seasons (explicit accounting for non-climate drivers) or implicitly account for their potential contributions by e.g., allowing

420   for non-climate related temporal trends in empirical models as often done in empirical approaches
(implicit accounting for non-climate drivers). In a second step, the impact model can be used to describe
the counterfactual world without long-term changes in the climate-related systems by forcing it with the
observed changes in direct human influences as in the evaluation experiments (see section **2.1**) but by
a counterfactual, stationary state of the climate-related systems (see **Table 3**). Attribution of climate

425   impacts to anthropogenic forcing would need an additional step separating anthropogenic climate
forcing from other sources of climate trends, which is not covered by the ISIMIP3a attribution setup.
Here, we describe the reasoning behind the individual experiments. Potentially required spin-up should
be identical to the corresponding 'obsclim' experiments mentioned in each description.

Standard attribution experiment using counterfactual climate-related forcings and observed

430   **variations of direct human forcings (counterclim + histsoc; default).** This is the twin experiment to
the default 'obsclim+histsoc' evaluation experiment. It uses the 'counterclim' climate-related forcings
as described in **Table 3** while all direct human forcings are the same as the ones used in the evaluation
experiment ('histsoc'). As the corresponding evaluation experiment aims to ensure that impact models
can fully capture the historical variations including its long-term trends, this experiment is best suited

435   for impact attribution. It is therefore the standard impact attribution experiment that each sector should
strive to follow.

Fixed 2015 direct human forcing attribution experiment (counterclim + 2015soc; default). This
is the twin experiment to the 'obsclim+2015soc' experiment. It uses the 'counterclim' climate-related

440   forcings as described in **Table 3** and constant direct human forcings at 2015 levels ('2015soc'). Impact
attribution using this experiment has caveats because the twin 'obsclim+2015soc' experiment is not
built to fully explain the historical observations including its trends. Impact attribution building on this
experiment therefore needs to find other means to ensure that the impact model correctly captures the
response to changes in the climate-related systems. It may e.g. build on the assumption that fixed direct

445   human forcings do not change the models' sensitivity to historical climate change. The impact models
that cannot account for varying historical direct human forcings can take up the attribution task through
this experiment.

Fixed 1901 direct human forcing attribution experiment (counterclim + 1901soc; default). This is

450   the twin experiment to the 'obsclim+1901soc' experiment. It allows for a quantification of the combined
effect of changes in all forcings (climate-related and direct human) during the historical period when
compared to the default evaluation experiment ('obsclim+histsoc'). It also allows for a quantification of
the effect of varying direct human drivers when compared to the 'counterclim+histsoc' experiment and
the effect of the 2015 to 1901 difference in direct human forcing if compared to the

455   'counterclim+2015soc' experiment, conditional on counterclim climate-related forcings.

No direct human forcing attribution experiment (counterclim + nat; default) This is the twin
experiment to the default 'obsclim+nat' experiment. It allows for a quantification of the effect of climate

change under conditions of absent direct human forcings but a natural state of the world. The 'nat'
460 experiment is included in the *biomes* sector protocol.

Table 4: ISIMIP3a attribution experiments

Experiment	Short description	Period: Historical 1901-2019
counterfactual climate histsoc **1st priority**	**CRF:** Detrended observational atmospheric climate forcing, detrended observed coastal water level forcings, and other CRF as listed in **Table 3**	**counterclim**
	DHF: Varying direct human influences according to observations	**histsoc**
counterfactual climate 2015soc **1st priority**	**CRF:** Detrended observational atmospheric climate forcing, detrended observed coastal water level forcings, and other CRF as listed in **Table 3**	**counterclim**
	DHF: Fixed 2015 levels of direct human forcing for the entire time period	**2015soc**
counterfactual climate 1901soc **2nd priority**	**CRF:** Detrended observational atmospheric climate forcing, detrended observed coastal water level forcings, and other CRF as listed in **Table 3**	**counterclim**
	DHF: Fixed 1901 levels of direct human forcing for the entire time period	**1901soc**
counterfactual climate nat **2nd priority**	**CRF:** Detrended observational atmospheric climate forcing, detrended observed coastal water level forcings, and other CRF as listed in **Table 3**	**counterclim**
	DHF: No direct human influences	**nat**

3 Climate-related forcing data

465

3.1 Observational atmospheric climate forcing data (factual + counterfactual)

Table 5: Atmospheric climate variables provided as part of the climate-related forcing

Variable	Variable specifier	Unit	Resolution	Datasets
Near-Surface Relative Humidity	**hurs**	%	0.5° grid, daily	GSWP3-W5E5 (factual and counterfactual, 1901-2019), 20CRv3-W5E5 (factual and counterfactual, 1901-2019), 20CRv3-ERA5 (factual and counterfactual, 1901-2021), 20CRv3 (factual and counterfactual, 1901-2015)
Near-Surface Specific Humidity	**huss**	kg kg-1	0.5° grid, daily	GSWP3-W5E5 (factual and counterfactual, 1901-2019), 20CRv3-W5E5 (factual and counterfactual, 1901-2019), 20CRv3-ERA5 (factual and counterfactual, 1901-2021), 20CRv3 (factual and counterfactual, 1901-2015)
Precipitation (including snowfall)	**pr**	kg m-2 s-1	0.5° grid, daily	GSWP3-W5E5 (factual and counterfactual, 1901-2019), 20CRv3-W5E5 (factual and counterfactual, 1901-2019), 20CRv3-ERA5 (factual and counterfactual, 1901-2021), 20CRv3 (factual and counterfactual, 1901-2015)
			30" grid, 90" grid, 300" grid, 1800" grid; daily	CHELSA-W5E5 (factual, 1979-2016)
Snowfall	**prsn**	kg m-2 s-1	0.5° grid, daily	GSWP3-W5E5 (factual only, 1901-2019, 0.5°)
Surface Air Pressure	**ps**	Pa	0.5° grid, daily	GSWP3-W5E5 (factual and counterfactual, 1901-2019), 20CRv3-W5E5 (factual and counterfactual, 1901-2019), 20CRv3-ERA5 (factual and counterfactual, 1901-2021), 20CRv3 (factual and counterfactual, 1901-2015)

Surface Downwelling Longwave Radiation	**rlds**	W m-2	0.5° grid, daily	GSWP3-W5E5 (factual and counterfactual, 1901-2019), 20CRv3-W5E5 (factual and counterfactual, 1901-2019), 20CRv3-ERA5 (factual and counterfactual, 1901-2021), 20CRv3 (factual and counterfactual, 1901-2015)
Surface Downwelling Shortwave Radiation	**rsds**	W m-2	0.5° grid, daily	GSWP3-W5E5 (factual and counterfactual, 1901-2019), 20CRv3-W5E5 (factual and counterfactual, 1901-2019), 20CRv3-ERA5 (factual and counterfactual, 1901-2021), 20CRv3 (factual and counterfactual, 1901-2015)
			30" grid, 90" grid, 300" grid, 1800" grid; daily	CHELSA-W5E5 (1979-2016)
Near-Surface Wind Speed	**sfcwind**	m s-1	0.5° grid, daily	GSWP3-W5E5 (factual and counterfactual, 1901-2019), 20CRv3-W5E5 (factual and counterfactual, 1901-2019), 20CRv3-ERA5 (factual and counterfactual, 1901-2021), 20CRv3 (factual and counterfactual, 1901-2015)
Near-Surface Air Temperature	**tas**	K	0.5° grid, daily	GSWP3-W5E5 (factual and counterfactual, 1901-2019), 20CRv3-W5E5 (factual and counterfactual, 1901-2019), 20CRv3-ERA5 (factual and counterfactual, 1901-2021), 20CRv3 (factual and counterfactual, 1901-2015)
			30" grid, 90" grid, 300" grid, 1800" grid; daily	CHELSA-W5E5 (1979-2016)

Daily Maximum Near-Surface Air Temperature	**tasmax**	K	0.5° grid, daily	GSWP3-W5E5 (factual and counterfactual, 1901-2019), 20CRv3-W5E5 (factual and counterfactual, 1901-2019), 20CRv3-ERA5 (factual and counterfactual, 1901-2021), 20CRv3 (factual and counterfactual, 1901-2015)
			30" grid, 90" grid, 300" grid, 1800" grid; daily	CHELSA-W5E5 (factual and counterfactual, 1979-2016)
Daily Minimum Near-Surface Air Temperature	**tasmin**	K	0.5° grid, daily	GSWP3-W5E5 (factual and counterfactual, 1901-2019), 20CRv3-W5E5 (factual and counterfactual, 1901-2019), 20CRv3-ERA5 (factual and counterfactual, 1901-2021), 20CRv3 (factual and counterfactual, 1901-2015)
			30" grid, 90" grid, 300" grid, 1800" grid; daily	CHELSA-W5E5 (1979-2016)

470   **Default factual data.** We provide four observational datasets specifically generated for the evaluation experiments of ISIMIP3a: GSWP3-W5E5, 20CRv3-W5E5, 20CRv3-ERA5, and 20CRv3. All four datasets have daily temporal and 0.5° spatial resolution. Their temporal coverage varies, with GSWP3-W5E5 and 20CRv3-W5E5 covering 1901-2019, while 20CRv3-ERA5 covers 1901-2021 and 20CRv3 covers 1901-2015. Instead of excluding datasets that do not cover the most recent years, we focussed

475   on including datasets that start in 1901, to allow for a common spin-up procedure (described in section **2.1** for the 'obsclim + histsoc; default' experiment), in order to support models that need to spin up, e.g., their carbon pools under stable climate-related and direct human forcings before they can do the actual experiments.

480   The GSWP3-W5E5 dataset is based on W5E5 v2.0 (Lange et al., 2021), which is also used as the observational reference dataset for the bias adjustment of climate input data for ISIMIP3b (Frieler et al., submitted 2023). W5E5 v2.0 combines WFDE5 v2.0 (WATCH Forcing Data methodology applied to ERA5 reanalysis data over land; Cucchi et al., 2020) with data from the latest version of the European Reanalysis (ERA5; Hersbach et al., 2020) over the ocean. Since W5E5 v2.0 only covers the years 1979

485   to 2019, it was extended backward in time to the year 1901. For this extension, we used version 1.09
        of the Global Soil Wetness Project phase 3 (GSWP) dataset (Kim, 2017), bias-adjusted to W5E5 v2.0
        in order to reduce discontinuities at the 1978–1979 transition. The method used for this bias adjustment
        was ISIMIP3BASD v2.5 (Lange, 2019, 2021). The GSWP3 dataset is a dynamically downscaled and
        bias-adjusted version of the Twentieth Century Reanalysis version 2 (20CRv2; Compo et al., 2011).
490   For a detailed description of the GSWP3-W5E5 dataset and its constituents, see Mengel et al., 2021.

        Unfortunately, for some variables, GSWP3 shows discontinuities at every turn of the month. The month-
        by-month bias adjustment applied in its creation is responsible for this artefact (Rust et al., 2015). In
        order to overcome this issue, which also affects GSWP3-W5E5, we additionally provide 20CRv3-
495   W5E5, a dataset where W5E5 v2.0 is backward-extended using ensemble member 1 of the Twentieth
        Century Reanalysis version 3 (20CRv3; Slivinski et al., 2019, 2021), interpolated to 0.5° and then bias-
        adjusted to W5E5 v2.0 using ISIMIP3BASD v2.5. The 20CRv3-W5E5 data are continuous at every turn
        of the month thanks to the application of ISIMIP3BASD v2.5 in running-window mode (see section **3.1**).
        Since GSWP3 is based on 20CRv2, the 20CRv3-W5E5 dataset can be considered an update of
500   GSWP3-W5E5.

        Two more climate input datasets are provided in ISIMIP3a in order to facilitate climate input data-related
        quantifications of uncertainty in the associated impact assessments. Those datasets are not based on
        W5E5 to account for trend and variability artefacts in W5E5 that are related to the climatological infilling
505   procedures used to deal with gaps in the station observations employed for the bias adjustment of
        ERA5 for the production of WFDE5 (for a detailed description of this caveat see
        https://data.isimip.org/caveats/20/). The first of the additional ISIMIP3a climate input datasets is
        20CRv3-ERA5, which was created in the same way as 20CRv3-W5E5, but using ERA5 instead of
        W5E5 for the time period 1979-2021, and also as the bias adjustment target for the time period 1901-
510   1978. Finally, we also provide the 'raw' 20CRv3 data, i.e., ensemble member 1 of 20CRv3, interpolated
        to 0.5° but not bias-adjusted to any other dataset. This dataset is included since it was generated with
        only one method and did not need to be combined with another dataset to fully cover the 20th century.

        Default counterfactual data. To simulate the baseline 'no climate change' state of a human or natural
515   system that is required for impact attribution, we provide a detrended version of the observational
        factual forcing data using the ATTRICI approach (ATTRIbuting Climate Impacts, Mengel et al., 2021).
        The method identifies the long-term shifts in the factual daily climate variables that are correlated to
        global mean temperature change assuming a smooth annual cycle of the associated scaling coefficients
        for each day of the year. We then remove these observed trends since 1901 from the observational
520   data by projecting the observed data onto the estimated distributions assuming a fixed 1901 level of
        global warming. The projection is done through quantile mapping, a method borrowed from the bias
        adjustment literature. In this way we preserve the internal variability of the observed data in the sense
        that factual and counterfactual data for a given day have the same rank in their respective statistical
        distributions. The impact model simulations forced by the counterfactual climate inputs therefore allow

525   for quantifying the contribution of the observed climate change (no matter from where the trends originate) to observed long-term changes in impact indicators but also for quantifying the contribution of the observed trend in climate to the magnitude of individual impact events.

High resolution atmospheric factual data (CHELSA-W5E5). This dataset is provided to facilitate the

530   high resolution sensitivity experiment described in section **2.1**. It covers the global land area at 30'' (~1 km) horizontal and daily temporal resolution from 1979 to 2016 for the variables precipitation (pr), surface downwelling shortwave radiation (rsds), and daily mean, minimum and maximum near-surface air temperature (tas, tasmin, tasmax). CHELSA-W5E5 v1.0 (Karger et al., 2022b) is a downscaled version of the W5E5 v1.0 dataset, where the downscaling is done with the Climatologies at High

535   resolution for the Earth's Land Surface Areas (CHELSA) v2.0 algorithm (Karger et al., 2017, 2021, 2022a).

This algorithm applies topographic adjustments based on surface altitude (orog) information from the Global Multi-resolution Terrain Elevation Data 2010 (GMTED2010; Danielson and Gesch, 2011). The

540   algorithm is applied day by day. CHELSA-W5E5 tas is obtained by applying a lapse rate adjustment to W5E5 tas, using differences between CHELSA-W5E5 orog and W5E5 orog in combination with temperature lapse rates from ERA5. Those lapse rates are calculated based on atmospheric temperature, T, at 950 hPa and 850 hPa, and the geopotential height, z, of those pressure levels. The lapse rate used for the adjustment is calculated as the daily mean of hourly values of $(T\_850 - T\_950)/$

545    $(z\_850 - z\_950)$. The variables tasmax and tasmin are downscaled in the same way, using the same lapse rate value.

Precipitation downscaling uses daily mean zonal and meridional wind components from ERA5 to approximate the orographic wind effect on small-scale precipitation patterns (differences between windward and leeward precipitation rates) and combines that with the height of the planetary boundary

550   layer to estimate the total orographic effect on precipitation intensity. Using that, precipitation from W5E5 is downscaled such that precipitation fluxes are preserved at the original 0.5° resolution of W5E5. More details are given in Karger et al., 2021.

Surface downwelling shortwave radiation, rsds, at 30 arcsec resolution is strongly influenced by topographic features such as aspect or terrain shadows, which are less pronounced at 0.5° resolution.

555   The downscaling algorithm combines such geometric effects with orographic effects on cloud cover for an orographic adjustment of rsds. Geometric effects are considered by computing 30'' clear-sky radiation estimates using the method described in Karger et al., 2022a and a simplified, uniform atmospheric transmittance of 80%. These effects include shadowing from surrounding terrain, diffuse radiation, and terrain aspect. To include how orographic effects on cloud cover influence rsds, the clear-

560   sky radiation estimates are adjusted using downscaled ERA5 total cloud cover. The cloud cover downscaling uses ERA5 cloud cover at all pressure levels and the orographic wind field following the methods described in Brun et al., 2022b. Finally, the clear-sky radiation estimates adjusted for cloud cover are rescaled such that they match W5E5 rsds, B-spline interpolated to 30''.

565 We provide the original CHELSA-W5E5 data with a horizontal resolution of 30'' = 0.5' (~1 km) as well as spatially aggregated versions with resolutions of 1.5' (~3 km, aggregation factor 3), 5.0' (~10 km, aggregation factor 10) and 30.0' = 0.5° (~60 km, aggregation factor 60). The aggregation to 0.5° is necessary since the aggregated CHELSA-W5E5 data differ from the default GSWP3-W5E5 and 20CRv3-W5E5 data provided in the 'obsclim' set-up for 1979-2016. This has two reasons. First, the downscaled data are based on W5E5 v1.0 whereas GSWP3-W5E5 and 20CRv3-W5E5 are based on

570 W5E5 v2.0. Secondly, for all variables except pr, the CHELSA downscaling algorithm produces data that differs from the original data when it is upscaled (spatially aggregated) back to the original resolution.

We do not provide a counterfactual version of the high resolution climate forcing.

575

The CHELSA method is not yet available for all variables included in the standard forcing data. Relative humidity, surface wind, air pressure, and longwave radiation can not yet be downscaled by the approach. To allow modellers to start the sensitivity experiments already now, we provide an alternative downscaling approach as described below. We use observational data with the required higher spatial

580 resolution but lower temporal resolution to generate the high resolution daily relative humidity and surface wind speeds. Air pressure is derived by on orographic correction of the linearly interpolated sea level pressure and surface downwelling longwave radiation is derived from high-resolution temperatures derived by CHELSA and relative humidity. The code required to generate the data is freely available (Malle, 2023).

585

For daily mean near-surface relative humidity (hurs) the provided downscaling algorithm combines monthly 30'' CHELSA-BIOCLIM+ data (Brun et al., 2022b, a) with daily W5E5 data. In a first step we regrid daily 0.5° W5E5 hurs to the target grid (30") by bilinear interpolation. We assume relative humidity to follow a beta-distribution and logit-transform both regridded monthly-averaged W5E5 ($hurs_{mon}^{W5E5}$) and

590 monthly CHELSA-BIOCLIM+ ($hurs_{mon}^{CHELSA}$) relative humidity data. The difference ($\Delta hurs_{mon}$) is then added to daily regridded and logit-transformed W5E5 hurs of the respective month, and the final raster is obtained by back-transforming the sum:

$$hurs_{dly} = \frac{1}{(1+exp^{-h})} \quad , (1)$$

where

595 $$h = log(\frac{hurs_{dly}^{W5E5}}{1-hurs_{dly}^{W5E5}}) + \Delta hurs_{mon} \quad , (2)$$

$$\Delta hurs_{mon} = log(\frac{hurs_{mon}^{CHELSA}}{1-hurs_{mon}^{CHELSA}}) - log(\frac{hurs_{mon}^{W5E5}}{1-hurs_{mon}^{W5E5}}) \cdot (3)$$

To include orographic effects into daily mean near-surface wind speed (*sfcwind*) we follow the approach of (Brun et al., 2022b), and use an aggregation of the Global Wind Atlas 3.0 data (Technical University

of Denmark, 2023) in combination with daily 0.5° sfcwind from W5E5. We first regrid both the Global

600 Wind Atlas data and the W5E5 sfcwind data to the target grid of 30'' using bilinear interpolation. The

Global Wind Atlas data product ($sfcWind_{cli}^{GWA}$) represents average wind speeds for 2008 to 2017. We

therefore average daily regridded W5E5 data over this time period ($sfcWind_{cli}^{W5E5}$). We assume surface

wind speeds follows a Weibull distribution and log-transform both datasets before computing the

difference $\Delta sfcWind_{cli}$, whereby a small positive constant (c) was added to all data points before

605 applying the transformation to avoid the problem that log(0) is undefined. We add this difference layer

($\Delta sfcWind_{cli}$) to each log-transformed daily W5E5 raster, and back-transform the sum to obtain the final

daily mean near-surface wind speed raster:

$$sfcWind_{dly} = exp^{(log(sfcWind_{dly}^{W5E5} + c) + \Delta sfcWind_{cli})} - c \text{ , (4)}$$

where

610 $$\Delta sfcWind_{cli} = log(sfcWind_{cli}^{GWA} + c) - log(sfcWind_{cli}^{W5E5} + c) \text{ . (5)}$$

Daily mean surface air pressure (ps) is calculated using the barometric formula:

$$ps_{dly} = psl_{dly}^{W5E5} \times exp^{-(g \times orog \times M)/(T_0 \times R)} \text{ , (6)}$$

with psl_{dly}^{W5E5} being the regridded 0.5° W5E5 daily mean sea-level pressure (bilinear interpolation to 30''),

615 g the gravitational acceleration constant (9.80665 m/s^2), *orog* the altitude at which air pressure is

calculated (CHELSA-W5E5 orog, m), *M* the molar mass of dry air (0.02896968 kg/mol), *R* the universal

gas constant (8.314462618 J/(mol K)) and T_0 the sea level standard temperature (288.16 K).

For Surface Downwelling Longwave Radiation (*rlds*) we follow Fiddes and Gruber, 2014 as well as

620 Konzelmann et al., 1994, and account for orographic effects by reducing the clear-sky component of

all-sky emissivity with elevation. We assume cloud emissivity remains unchanged when moving from

coarse to fine resolution. First, we compute clear-sky emissivity components both for the 0.5° W5E5

grid and the target 30'' grid (ϵ_{clear}^{W5E5}, $\epsilon_{clear}^{highres}$ respectively):

$$\epsilon_{clear}^{highres/W5E5} = 0.23 + x1(pV_{dly}^{highres/W5E5}/ tas_{dly}^{highres/W5E5})^{1/x2} \text{ , (7)}$$

625 where x1 = 0.43 and x2 = 5.7 and $pV_{dly}^{highres/W5E5}$ is water vapour pressure as a function of relative

humidity at the respective resolution (see Fiddes and Gruber, 2014). By using 0.5° W5E5 *rlds* and *tas*

data and inverting the Stefan-Boltzmann equation we obtain all-sky emissivity:

$$\epsilon_{allsky}^{W5E5} = rlds_{dly}^{W5E5}/ (\sigma \times (tas_{dly}^{W5E5})^4) \text{ , (8)}$$

with σ being the Stefan-Boltzmann constant (5.67 x 10^{-8} Js^{-1} m^{-2} K^{-4}). In a next step, the cloud-based

630   component of emissivity ($\Delta\epsilon_{dly}^{W5E5}$) can be estimated as the difference between all-sky and clear-sky

emissivity, which is then regridded to the target grid via bilinear interpolation.

$$\Delta\epsilon_{dly}^{W5E5} = \epsilon_{allsky}^{W5E5} - \epsilon_{clear}^{W5E5} \quad (9)$$

In a last step we obtain elevation-corrected longwave radiation ($rlds_{dly}$) by adding $\Delta\epsilon_{dly}^{W5E5}$ to the high-

resolution clear-sky emissivity ($\epsilon_{clear}^{highres}$) and applying the Stefan-Boltzmann law again:

635   $$rlds_{dly} = (\epsilon_{clear}^{highres} + \Delta\epsilon_{dly}^{W5E5}) \times \sigma \times (tas_{dly}^{highres})^4 \quad (10)$$

As soon as the CHELSA approach is extended to also cover the missing variable we plan to also provide these data and test for the sensitivity of the impact simulations to these two alternative downscaling methods.

640   **3.2 Tropical cyclone (TC) data (factual)**
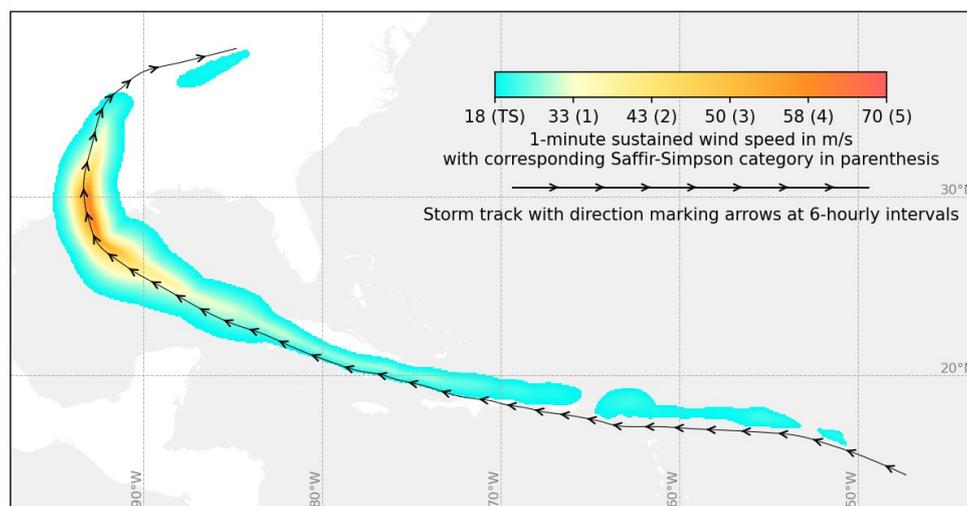
Figure 2: Tropical cyclone storm track (line with arrows) and derived maximum wind speeds (coloured shades, according to the Holland wind profile, Holland, 1980, 2008) of major hurricane Laura that made landfall in
645   Louisiana (USA) in August 2020.

Table 6: Tropical cyclone information provided as part of the ISIMIP3a climate-related forcing

Variable	Variable specifier	Unit	Resolution	Datasets

Time associated with a given location of the storm centre	**time**	hours since 1950-01-01 00:00	along-track, at least 3-hourly	IBTrACS (1950-2021, postprocessed)
Latitudinal/ longitudinal coordinate of storm centre (as defined by the reporting agencies)	**lat** **lon**	degrees north/ east	along-track, at least 3-hourly	IBTrACS (1950-2021, postprocessed)
Ocean basin: NA/SA (North/South Atlantic), EP/WP/SP (East/West/South Pacific), NI/SI (North/South Indian Ocean)	**basin**	two-letter abbreviation	along-track, at least 3-hourly	IBTrACS (1950-2021, postprocessed)
Central pressure	**pres**	hPa	along-track, at least 3-hourly	IBTrACS (1950-2021, postprocessed)
Environmental pressure (pressure of the outermost closed isobar)	**penv**	mbar	along-track, at least 3-hourly	IBTrACS (1950-2021, postprocessed)
Maximum 1-minute sustained wind speed	**wind**	knots	along-track, at least 3-hourly	IBTrACS (1950-2021, postprocessed)
Radius of maximum wind speeds	**rmw**	nautical miles	along-track, at least 3-hourly	IBTrACS (1950-2021, postprocessed)
Radius of the outermost closed isobar	**roci**	nautical miles	along-track, at least 3-hourly	IBTrACS (1950-2021, postprocessed)
Wind speed on the 850 hPa pressure level	**u850** **v850**	ms^-1	along-track, at least 3-hourly	IBTrACS (1950-2021, postprocessed)
Temperature on the 600 hPa pressure level	**T600**	K	along-track, at least 3-hourly	IBTrACS (1950-2021, postprocessed)

1-minute sustained wind speed	**wind**	ms^-1	along-track, at least 3-hourly on a 300 arc-seconds (~10 km) grid	according to the Holland wind profile (Holland, 1980, 2008) and the Emanuel-Rotunno wind profile (Emanuel and Rotunno, 2011)
Maximum 1-minute sustained wind speed during the whole storm duration	**max_wind**	ms^-1	for each TC on a 300 arc-seconds (~10 km) grid	according to the Holland wind profile (Holland, 1980, 2008) and the Emanuel-Rotunno wind profile (Emanuel and Rotunno, 2011)
National territory exposed to wind speeds of at least 34, 48, 64, 96 knots	**34kn_area** **48kn_area** **64kn_area** **96kn_area**	km^2	for each TC and country	according to the Holland wind profile (Holland, 1980, 2008) and to the Emanuel-Rotunno wind profile (Emanuel and Rotunno, 2011)
Number of people exposed to wind speeds of at least 34, 48, 64, 96 knots	**34kn_pop** **48kn_pop** **64kn_pop** **96kn_pop**	count	for each TC and country	according to the Holland wind profile (Holland, 1980, 2008) and to the Emanuel-Rotunno wind profile (Emanuel and Rotunno, 2011) and assuming temporally varying (histsoc) or fixed 2015 (2015soc) population distributions (see section **4.1**).
Economic assets exposed to wind speeds of at least 34, 48, 64, 96 knots	**34kn_assets** **48kn_assets**	Int$ PPP 2005	for each TC and country	Windfields according to the Holland wind profile (Holland, 1980, 2008) and Emanuel-Rotunno

	64kn_assets 96kn_assets			wind profile (Emanuel and Rotunno, 2011) and assuming temporally varying (histsoc) or fixed 2015 (2015soc) asset distributions (see section **4.2**).
rainfall	**rain**	mm	along-track, at least 3-hourly on a 300 arc-seconds (~10 km) grid	according to the Holland wind profile (Holland, 1980, 2008) and to the Emanuel-Rotunno wind profile (Emanuel and Rotunno, 2011)
Maximum 24-hourly rainfall during the whole storm duration	**max_rain**	mm	for each TC on a 300 arc-seconds (~10 km) grid	according to the Holland wind profile (Holland, 1980, 2008) and to the Emanuel-Rotunno wind profile (Emanuel and Rotunno, 2011)

As additional CRF, we provide historical TC tracks (information about the observed location of minimal pressure), associated gridded wind and rain fields. In addition to this purely CRF, we also provide wind exposure in terms of (i) shares of national territory affected by extreme winds speeds, (ii) national shares of people exposed to extreme winds speeds, and (iii) national shares of economic assets affected by extreme winds speeds as derived from the estimated wind fields and historical population and GDP distributions (see below).

TC Tracks (position of storm centre, central pressure, environmental pressure, radius of maximum wind speed and the outermost closed isobar). We provide processed track information of historical TCs from 1950 to 2021. The information is derived from IBTrACS, the most comprehensive global dataset of historical TC activity (Knapp et al., 2010) that provides information about the location of the storm centre, the pressure at the centre and at the outermost closed isobar as well as the maximum 1-minute sustained wind speed as reported by the WMO Regional Specialised Meteorological Centers (RSMCs) and by agencies in Shanghai and Hong Kong. For recent events and most reporting agencies, IBTrACS also contains observational information about the radius from the centre where maximum wind speed is attained and the radius of the outermost closed isobar. Information is provided

in at least 6-hourly time steps. Usually temporal resolution reaches three hours or even less. The latest version (v04r00) of IBTrACS is continuously updated with near real time data taken from regional
665   meteorological agencies. The data is marked as provisional before it is replaced by so-called best track data one up to two years after the events. IBTrACS contains data from 1842 to present, but coverage by the WMO RSMCs starts much later for some of the basins (around 1850 for the North Atlantic and South Indian, in 1905 for the South Pacific, in 1950 for the North Pacific, and in 1990 for the Northern Indian basin). Data quality is globally consistent starting from the mid 1970s when satellite observations
670   became available.

The data set we provide uses best track data from 1950 to 2021. For each TC in IBTrACS, we merge the data of different reporting agencies into a single track data set with information about the following variables: time, location of the storm centre, ocean basin, central pressure, maximum 1-minute sustained wind speed, environmental pressure, radius of maximum wind speeds, and radius of the
675   outermost closed isobar (see Table 8). Several processing steps are applied to ensure consistency and completeness of the data: For each storm, the variables that are not reported by the officially responsible WMO RSMC for this storm are taken from the next agency in the following list that did report this variable for this storm: the US agencies (NHC, JTWC, CPHC), Japanese Meteorological Agency, Indian Meteorological Department, MeteoFrance (La Reunion), Bureau of Meteorology (Australia), Fiji
680   Meteorological Service, New Zealand MetService, Chinese Meteorological Administration, Hong Kong Observatory. Thus, for different storms, the same variable might be taken from different agencies. As sustained wind speeds are reported at different averaging intervals by different agencies, we use multiplicative factors to rescale all wind speeds to 1-minute sustained winds (Knapp and Kruk, 2010). All variables are extracted at the highest temporal resolution where time and location information is
685   available in IBTrACS. Temporal reporting gaps within a variable are linearly interpolated so that the temporal resolution is at least 3-hourly. After interpolation, time steps where neither central pressure nor maximum wind speeds are available, are discarded. Tracks with less than two valid time steps are discarded. If at least one of central pressure or maximum wind speed is available, one variable is estimated from the other using statistical wind-pressure relationships. Missing RMW and ROCI values
690   are estimated from the central pressure using statistical relationships. Finally, missing environmental pressure values are filled with basin-specific defaults (1010 hPa for the Atlantic and Eastern Pacific, 1005 hPa for the Indian Ocean and Western Pacific, and 1004 hPa for the South Pacific).

We provide two additional along-track variables that are taken from the European Reanalysis (ERA5; Hersbach et al., 2020), and that are needed for the computation of precipitation (see below): The
695   temperature at the storm centre on the 600 hPa pressure level, and the wind speed on the 850 hPa pressure level, averaged over the 200-500 km annulus around the storm centre.

Gridded maps of (maximum) wind speeds. We derive two different gridded wind field products from an extrapolation of the observed TC track information to gridded estimates of surface wind speeds (1-minute sustained winds at 10 metres above ground), at a spatial resolution of 300 arc-seconds
700   (approximately 10 km). The two products are based on circular wind fields from different radial wind profiles. The first is a semiempirical model that estimates the full wind profile from the central pressure

variable based on the gradient wind balance assumption (Holland, 1980, 2008). The second, more physics-based model uses the less-reliable maximum wind speed variable to derive the wind profile from the boundary layer angular momentum balance (Emanuel and Rotunno, 2011). This wind profile 705 represents the storm's inner core very well, but tails off too sharply in the outer region (Chavas and Lin, 2016). However, for high-impact events, the core is the most relevant storm region, and outer wind profiles are not analytically solvable, incurring considerable computational expense when applied to a large track set.

710 In both cases, the circular wind fields are combined with translational wind vectors that arise from the TC movement, assuming that the influence of translational wind decreases with distance from the TC centre (Mouton and Nordbeck 2005). We use the highest available temporal resolution (up to 3-hourly) provided in IBTrACS and interpolate it to 1-hourly resolution before applying the parametric wind field models. In a postprocessing step, we also calculate the maximum value of wind speeds over the 715 duration of the TC event ('max_wind').

The approach by Holland has been successfully applied in socioeconomic risk and impact analyses (Peduzzi et al., 2012; Geiger et al., 2018; Eberenz et al., 2021). The Emanuel-Rotunno approach has been used for storm surge simulations (Krien et al., 2017; Marsooli et al., 2019; Gori et al., 2020; Yang et al., 2021), and as the basis for the rain field model that we describe below (Feldmann et al., 2019).

720 **Wind Exposure.** As an extension of the tropical cyclone exposure data set TCE-DAT (Geiger et al., 2018), we provide national shares of people and economic assets exposed to 1-minute sustained winds above 34, 48, 64, and 96 knots for each storm. In addition to that, shares of national territory affected by 1-minute sustained winds above 34, 48, 64, and 96 knots are provided. To estimate the exposed population and assets we use the 'histsoc' population and GDP distributions described in section **4.1** 725 and section **4.2**, respectively. The GDP values are converted to assets by applying the decadal (2010-2019) mean of national capital stock to GDP ratios from the Penn World Table version 10.0 (Feenstra et al., 2015). We also provide exposed population and assets assuming fixed 2015 population and asset distributions.

Precipitation. We are also planning to provide rainfall fields, following a physics-based model that 730 simulates convective TC rainfall by relating the precipitation rate to the total upward velocity within the TC vortex (Zhu et al., 2013). The approach has been successfully applied in rainfall risk assessments in the US (Feldmann et al., 2019; Gori et al., 2022). The rain rate will be simulated for all events in the IBTrACS database at 2-hourly temporal and 300 arc-seconds (approximately 10 km) spatial resolution within the storm extent defined by the ROCI storm track variable. We will also aggregate the result to 735 the maximum 24-hourly rainfall during the entire storm duration since this variable is frequently used for rainfall risk assessment studies (Fagnant et al., 2020).

Different TC wind profiles can be used as an input for the rain field model (Lu et al., 2018; Xi et al., 2020). We will provide the rainfall fields for the two wind profile models by Holland and Emanuel-Rotunno that we also use for the wind fields described above.

3.3 Coastal water levels (factual + counterfactual)
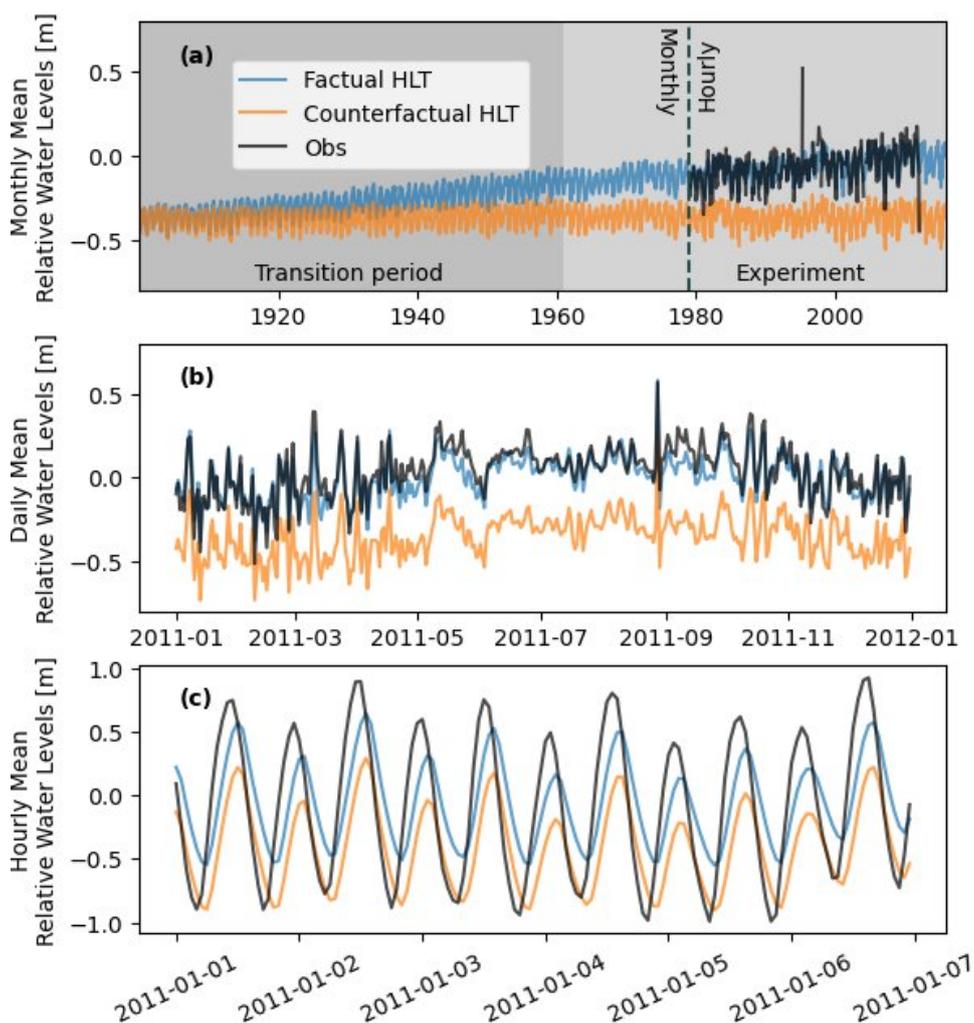
745 **Figure 3: Observed and reconstructed coastal relative water levels** at New York, USA. The counterfactual baseline represents water levels without long-term trend since 1900. Water levels are aggregated to monthly means in panel (a) and daily means in the year 2011 in panel (b) while panel c shows part of the data in hourly resolution. The reconstructed water levels are available as monthly mean values from 1900 to 1979 and as hourly mean values from 1979 to 2015.

750

Table 7: Information about coastal water levels provided as ISIMIP3a climate-related forcing.

Variable	Variable specifier	Unit	Resolution	Datasets

Coastal water levels	**cwl**	m	custom coastal grid; monthly from 1901 to 1978 and hourly from 1979 to 2015	HLT obsclim and counterclim (Treu et al., submitted 2023)

To enable the quantification of impacts of historical relative sea level rise on coastal systems we provide observation-based coastal water levels building on the HLT (Hourly sea-level change with long-term trends for impact attribution; Treu et al., submitted 2023). In contrast to absolute sea levels, relative sea levels are measured against a land-based reference frame (tide gauge measurements). This means that they are not only determined by thermal expansion, loss of land ice, or dynamical processes influenced by climate change, but also by vertical land movements (Wöppelmann and Marcos, 2016) induced by, e.g., glacial isostatic adjustments (Caron et al., 2018; Whitehouse, 2018) or human interventions such as ground water abstraction (Wada et al., 2016a). HLT encompasses factual and counterfactual coastal water levels along global coastlines from 1901 to 1978 on monthly resolution and from 1979 to 2015 on hourly resolution. The counterfactual is derived from the factual dataset by removing the trend in relative sea level since 1900. The detrending preserves the timing of historical extreme sea-level events similar to the counterfactual atmospheric climate forcing described in section **3.1**. Hence, the data can be used for an event-based attribution of, e.g., observed flooding to observed relative sea-level rise with tuples of impact simulations driven with the factual and counterfactual dataset. It is important to highlight that 'attribution to observed changes in relative water levels' does not imply attribution to anthropogenic climate forcing because such observed changes may include trends that are not driven by human greenhouse gas emissions. Important sources for such trends are the ongoing adjustments of ice sheets, glaciers and the earth crust to climate conditions before industrialization (Slangen et al. 2016) and the land subsidence due to water, gas and oil extraction (Nicholls et al. 2021). In the following the derivation of the data is described in more detail.

Default factual data. To capture the impacts of extreme water levels we provide hourly observation-based coastal water levels as forcing data. To this end we combine the Coastal Dataset for the Evaluation of Climate Impact (CoDEC) dataset (Muis et al., 2020) that describes high frequency variation of sea level along global coastlines with a recent reconstruction of observed long-term sea-level rise (Dangendorf et al., 2019). The CoDEC hourly data builds on a shallow-water model with fixed ocean density driven by ERA5 wind and atmospheric pressure fields. The CoDEC data thus starts only in the year 1979 and does not include variations due to ocean density changes and multi-year trends from observed sea-level rise or vertical land movement. In contrast, the hybrid reconstructions (HR) dataset from Dangendorf et al., 2019 represents sea-level change since 1900 on a monthly timescale, including density variations and multi-year trends. Long term sea-level change in HR is based on fitting theoretically known and modelled spatial-temporal fields of individual contributing factors of sea level change to a set of observations of sea level change from tide gauges. The individual contributing factors are theoretically known cryospheric fingerprints from two ice sheets, 18 major glacier regions, glacial isostatic adjustment from 161 Earth rheological models and dynamic changes of sea surface height modelled by six global climate models. Short term sea-level variations are represented in HR by

extending the spatio-temporal patterns from satellite altimetry back to the year 1900 using tide gauge
790 records. We create the HLT dataset by low-pass filtering the HR dataset and high-pass filtering the
CoDEC dataset before summing them. HLT shows improved agreement with tide gauge records on
hourly to monthly time scales when compared to CoDEC due to the inclusion of density variations. This
is most apparent for lower latitudes. The performance on interannual time scales is equal to Dangendorf
et al., 2019.

795

Default counterfactual data. To estimate the effects of historical sea-level rise on coastal systems,
we provide a counterfactual sea-level dataset as forcing for coastal impact models (Treu et al.,
submitted 2023). To this end the long term trend in the HLT data (1900-2015) was identified by a simple
quadratic model in time and subtracted from the factual HLT data. The quadratic model assumes a
800 constant acceleration of sea-level rise over time. Analysis of sea level rise acceleration shows variation
throughout the last century with an acceleration phase in the early century followed by a deceleration
and then again acceleration until today (Dangendorf et al., 2019). By design, this variation is not
included in our quadratic trend estimate. In general, we expect our trend estimation to largely exclude
natural variability from the trend due to the low dimensionality of the trend model and the long data
805 period. This is a desired outcome and preserves the natural variability in the counterfactual. Extreme
sea-level events have the same timing in the counterfactual and the factual dataset, facilitating event-
based impact attribution.

3.4 Ocean data (factual)

810

Default factual data. For the fisheries and marine ecosystem models, we provide a number of physical
and biogeochemical variables for the period 1961 to 2010 at different depth levels in the ocean (see
Table 10). Since direct measurements of these variables are very scarce (Sarmiento and Gruber, 2006;
WOCE Atlas, 2023), the only way to obtain a globally (or even regionally) complete and consistent
815 forcing dataset is to use numerical models. Global ocean models, which also serve as oceanic
components of Earth System models, often simulate many or all of the required variables. To let
observations at least indirectly enter the oceanic forcing data for ISIMIP3a, we provide outputs from an
ocean model run that is forced by an observation-based reanalysis product of atmospheric forcing (Liu
et al., 2021). Compared to the oceanic forcing (Stock et al., 2014) provided to generate the ISIMIP2a
820 simulations for the *marine ecosystems and fisheries* sector (Tittensor et al., 2018), this new dataset is
based on the latest GFDL-MOM6 and COBALTv2 physical and biogeochemical ocean models running
on a tripolar 0.25° grid and using the JRA-55 reanalysis (Tsujino et al., 2018) as the surface forcing, in
contrast to the inter-annual forcing dataset of Large and Yeager, 2009, which was previously used to
drive GFDL-MOM4. The simulations also account for dynamic, time-varying river freshwater and
825 nitrogen inputs that were simulated based on GFDL's land-watershed model LM3-TAN (Land Model
version 3 with Terrestrial and Aquatic Nitrogen; Lee et al., 2019), adjusted using observations from the
Global Nutrient Export from WaterSheds (NEWS) database (Seitzinger et al., 2006). To create the
default 'obsclim' climate-related forcings for the fisheries and marine ecosystem models these ocean

830   model simulation data have been interpolated to a regular 0.25° grid while vertical resolution is preserved. In contrast to the atmospheric data, oceanic CRF are provided at monthly temporal resolution

Low resolution factual data. To test to what degree a lower spatial resolution of the climate-related forcings affects the impact model simulations, the oceanic climate-related forcings have also been
835   aggregated to one degree resolution as input for the 'obsclim + histsoc, 60arcmin' sensitivity experiment.

CRF for the '1955-riverine-input' sensitivity experiment. The '1955-riverine-inputs' sensitivity experiment builds on 0.25 degree GFDL-COBALT2 simulation forced by the JRA-55 reanalysis, but
840   without time-varying riverine inputs. Instead the influx of freshwater and nutrients are fixed at mean 1951 to 1958 levels as described in the "control run" introduced by Liu et al., 2021. The data is interpolated to a regular 0.25 degree grid in the same way as the default 'obsclim' CRFs.

We currently do not provide counterfactual versions of the ocean data forcing, though options are being
845   explored.

Table 8: ISIMIP3a oceanic climate-related forcing. Variables with suffixes -bot, -surf, and -vint were obtained from the seafloor, the top layer of the ocean, and vertical integration, respectively.

Variable	Variable specifier	Unit	Resolution	Datasets
Mass concentration of total phytoplankton expressed as chlorophyll	**chl**	kg m-3	0.25° and 1° grid, 35 levels (m from the surface), monthly	GFDL-COBALT2 simulation forced by the JRA-55 reanalysis, accounting for climate-driven changes in riverine inputs ('default') or assuming fixed levels of riverine inputs ('1955-riverine-input'). Standard salt water density of 1035 kg m-3 applied when converting from mass to volumetric unit, i.e. µg kg-1 to kg m-3
Downward flux of organic particles expressed as organic carbon at ocean bottom	**expc-bot**	mol m-2 s-1	0.25° and 1° grid, monthly	GFDL-COBALT2 simulation forced by the JRA-55 reanalysis, accounting for climate-driven changes in riverine inputs ('default') or assuming fixed levels of riverine inputs ('1955-riverine-

				input'). Derived from nitrogen detritus flux at ocean bottom (fndet_btm) by multiplying with fixed N-C ratio of 6.625. Extractions for individual grid cells available in ASCII format for regional models (see **Table 1**).
Particulate organic carbon content in the upper 100 m	**intpoc**	kg m-2	0.25° and 1° grid, monthly	GFDL-COBALT2 simulation forced by the JRA-55 reanalysis, accounting for climate-driven changes in riverine inputs ('default') or assuming fixed levels of riverine inputs ('1955-riverine-input'). Derived by aggregating bacterial, detritus, diazotroph, large+small phytoplankton, large+medium+small zooplankton nitrogen biomass and multiplying by a fixed N-C ratio of 6.625. Extractions for individual grid cells available in ASCII format for regional models (see **Table 1**).
Net primary organic carbon production by all types of phytoplankton in grid cell column	**intpp**	mol m-2 s-1	0.25° and 1° grid, monthly	GFDL-COBALT2 simulation forced by the JRA-55 reanalysis, both accounting for climate-driven changes in riverine inputs ('default') or assuming fixed levels of riverine inputs ('1955-riverine-input'). Derived by aggregating net primary productions by diatoms, diazotrophs and pico-phytoplankton and under the assumption of a fixed N-C ratio of 6.625. Extractions for individual grid cells

				available in ASCII format for regional models (see **Table 1**).
Net primary organic carbon production by diatoms in grid cell column	**intppdiat**	mol m-2 s-1	0.25° and 1° grid, monthly	GFDL-COBALT2 simulation forced by the JRA-55 reanalysis, both accounting for climate-driven changes in riverine inputs ('default') or assuming fixed levels of riverine inputs ('1955-riverine-input'). Derived under the assumption of a fixed N-C ratio of 6.625. Extractions for individual grid cells available in ASCII format for regional models (see **Table 1**).
Net primary organic carbon production of carbon by diazotrophs in grid cell column	**intppdiaz**	mol m-2 s-1	0.25° and 1° grid, monthly	GFDL-COBALT2 simulation forced by the JRA-55 reanalysis, both accounting for climate-driven changes in riverine inputs ('default') or assuming fixed levels of riverine inputs ('1955-riverine-input'). Derived under the assumption of a fixed N-C ratio of 6.625. Extractions for individual grid cells available in ASCII format for regional models (see **Table 1**).
Net Primary Mole Productivity of Carbon by Picophytoplankton in grid cell column	**intpppico**	mol m-2 s-1	0.25° and 1° grid, monthly	GFDL-COBALT2 simulation forced by the JRA-55 reanalysis, both accounting for climate-driven changes in riverine inputs ('default') or assuming fixed levels of riverine inputs ('1955-riverine-input'). Derived under the

				assumption of a fixed N-C ratio of 6.625.
Mixed Layer Ocean Thickness defined by a Sigma Theta difference (= density difference) of 0.125 kg m-3 compared to the surface	**mlotst-0125**	m	0.25° and 1° grid, monthly	GFDL-COBALT2 simulation forced by the JRA-55 reanalysis, both accounting for climate-driven changes in riverine inputs ('default') or assuming fixed levels of riverine inputs ('1955-riverine-input')
Dissolved oxygen concentration; vertically resolved, at the bottom or at the surface, respectively	**o2, o2-bot, o2-surf**	mol m-3	0.25° and 1° grid, 35 levels (m from the surface), monthly	GFDL-COBALT2 simulation forced by the JRA-55 reanalysis, both accounting for climate-driven changes in riverine inputs ('default') or assuming fixed levels of riverine inputs ('1955-riverine-input'). Extractions for individual grid cells of the bottom and surface layer available in ASCII format for regional models (see **Table 1**).
pH; vertically resolved, at the bottom or at the surface, respectively	**ph, ph-bot, ph-surf**	1	0.25° and 1° grid, 35 levels (m from the surface), ocean bottom and surface fields, monthly	GFDL-COBALT2 simulation forced by the JRA-55 reanalysis, both accounting for climate-driven changes in riverine inputs ('default') or assuming fixed levels of riverine inputs ('1955-riverine-input') where pH is derived from ion concentrations H+ as pH = -$\log_{10}$(H+). Extractions for individual grid cells of the bottom and surface layer available in ASCII format for regional models (see **Table 1**).

Total phytoplankton carbon concentration; vertically resolved or integrated over the grid cell column, respectively	**phyc, phyc-vint**	mol m-3	0.25° and 1° grid, 35 levels (m from the surface) and vertically integrated, monthly	GFDL-COBALT2 simulation forced by the JRA-55 reanalysis, both accounting for climate-driven changes in riverine inputs ('default') or assuming fixed levels of riverine inputs ('1955-riverine-input'). Aggregated from diatom, diazotroph and pico-phytoplankton. Standard salt water density of 1035 kg m-3 and fixed N-C ratio of 6.625 applied when converting from mass to volumetric unit, i.e. mol kg-1 to mol m-3. Extractions for individual grid cells of the vertically integrated data set are available in ASCII format for regional models (see **Table 1**).
Concentration of diatoms expressed as carbon in sea water; vertically resolved or integrated over the grid cell column, respectively	**phydiat, phydiat-vint**	mol m-3	0.25° and 1° grid, 35 levels (m from the surface) and vertically integrated, monthly	GFDL-COBALT2 simulation forced by the JRA-55 reanalysis, both accounting for climate-driven changes in riverine inputs ('default') or assuming fixed levels of riverine inputs ('1955-riverine-input'). Standard salt water density of 1035 kg m-3 and fixed N-C ratio of 6.625 applied when converting from mass to volumetric unit, i.e. mol kg-1 to mol m-3. Extractions for individual grid cells of the vertically integrated data set are available in ASCII format for regional models (see **Table 1**).

Concentration of diazotrophs expressed as carbon in sea water; vertically resolved or integrated over the grid cell column, respectively	**phydiaz, phydiaz-vint**	mol m-3	0.25° and 1° grid, 35 levels (m from the surface) and vertically integrated, monthly	GFDL-COBALT2 simulation forced by the JRA-55 reanalysis, both accounting for climate-driven changes in riverine inputs ('default') or assuming fixed levels of riverine inputs ('1955-riverine-input'). Standard salt water density of 1035 kg m-3 and fixed N-C ratio of 6.625 applied when converting from mass to volumetric unit, i.e. mol kg-1 to mol m-3.
Mole concentration of picophytoplankton expressed as carbon in sea water; vertically resolved or integrated over the grid cell column, respectively	**phypico, phypico-vint**	mol m-3	0.25° and 1° grid, 35 levels (m from the surface) and vertically integrated, monthly	GFDL-COBALT2 simulation forced by the JRA-55 reanalysis, both accounting for climate-driven changes in riverine inputs ('default') or assuming fixed levels of riverine inputs ('1955-riverine-input'). Standard salt water density of 1035 kg m-3 and fixed N-C ratio of 6.625 applied when converting from mass to volumetric unit, i.e. mol kg-1 to mol m-3.
Net downward shortwave radiation at sea water surface	**rsntds**	W m-2	0.25° and 1° grid, monthly	From JRA-55 reanalysis
Sea ice area fraction	**siconc**	%	0.25° and 1° grid, monthly	From JRA-55 reanalysis
Sea water salinity; vertically resolved, at the bottom, or at the surface, respectively	**so, so-bot, so-surf**	0.001	0.25° and 1° grid, 35 levels (m from the surface), ocean bottom and surface fields, monthly	GFDL-COBALT2 simulation forced by the JRA-55 reanalysis, both accounting for climate-driven changes in riverine inputs ('default') or assuming fixed levels of riverine inputs ('1955-riverine-input'). Extractions for individual grid cells of the surface and bottom layer are

				available in ASCII format for regional models (see **Table 1**).
Sea water potential temperature	**thetao**	°C	0.25° and 1° grid, 35 levels (m from the surface), monthly	GFDL-COBALT2 simulation forced by the JRA-55 reanalysis, both accounting for climate-driven changes in riverine inputs ('default') or assuming fixed levels of riverine inputs ('1955-riverine-input')
Ocean model cell thickness	**thkcello**	m	0.25° and 1° grid, 35 levels (m from the surface), constant	GFDL-COBALT2 simulation forced by the JRA-55 reanalysis, both accounting for climate-driven changes in riverine inputs ('default') or assuming fixed levels of riverine inputs ('1955-riverine-input')
Sea water potential temperature at sea floor (bottom)	**tob**	°C	0.25° and 1° grid, monthly	GFDL-COBALT2 simulation forced by the JRA-55 reanalysis, both accounting for climate-driven changes in riverine inputs ('default') or assuming fixed levels of riverine inputs ('1955-riverine-input'). Extractions for individual grid cells are available in ASCII format for regional models (see **Table 1**).
Sea surface temperature	**tos**	°C	0.25° and 1° grid, monthly	GFDL-COBALT2 simulation forced by the JRA-55 reanalysis, both accounting for climate-driven changes in riverine inputs ('default') or assuming fixed levels of riverine inputs ('1955-riverine-input'). Extracted from uppermost ocean layers potential

				temperatures. Extractions for individual grid cells are available in ASCII format for regional models (see **Table 1**).
Sea water zonal velocity	**uo**	m s-1	0.25° and 1° grid, 35 levels (m from the surface), monthly	GFDL-COBALT2 simulation forced by the JRA-55 reanalysis, both accounting for climate-driven changes in riverine inputs ('default') or assuming fixed levels of riverine inputs ('1955-riverine-input')
Sea water meridional velocity	**vo**	m s-1	0.25° and 1° grid, 35 levels (m from the surface), monthly	GFDL-COBALT2 simulation forced by the JRA-55 reanalysis, both accounting for climate-driven changes in riverine inputs ('default') or assuming fixed levels of riverine inputs ('1955-riverine-input')
Concentration of zooplankton of meso size expressed as carbon in seawater; vertically resolved or integrated over the grid cell column, respectively	**zmeso, zmeso-vint**	mol m-3	0.25° and 1° grid, 35 levels (m from the surface) and vertically integrated, monthly	GFDL-COBALT2 simulation forced by the JRA-55 reanalysis, both accounting for climate-driven changes in riverine inputs ('default') or assuming fixed levels of riverine inputs ('1955-riverine-input'). Aggregated from large and medium zooplankton. Standard salt water density of 1035 kg m-3 and fixed N-C ratio of 6.625 applied when converting from mass to volumetric unit, i.e. mol kg-1 to mol m-3. Extractions for individual grid cells of the vertically integrated data set are available in ASCII format for regional models (see **Table 1**).

Concentration of zooplankton of micro scale expressed as carbon in seawater; vertically resolved or integrated over the grid cell column, respectively.	**zmicro, zmicro-vint**	mol m-3	0.25° and 1° grid, 35 levels (m from the surface) and vertically integrated, monthly	GFDL-COBALT2 simulation forced by the JRA-55 reanalysis, both accounting for climate-driven changes in riverine inputs ('default') or assuming fixed levels of riverine inputs ('1955-riverine-input'). Standard salt water density of 1035 kg m-3 and fixed N-C ratio of 6.625 applied when converting from mass to volumetric unit, i.e. mol kg-1 to mol m-3. Extractions for individual grid cells of the vertically integrated data set are available in ASCII format for regional models (see **Table 1**).
Total Zooplankton Carbon Concentration; vertically resolved or integrated over the grid cell column, respectively	**zooc, zooc-vint**	mol m-3	0.25° and 1° grid, 35 levels (m from the surface) and vertically integrated, monthly	GFDL-COBALT2 simulation forced by the JRA-55 reanalysis, both accounting for climate-driven changes in riverine inputs ('default') or assuming fixed levels of riverine inputs ('1955-riverine-input'), aggregated from large, medium and micro zooplankton. Standard salt water density of 1035 kg m-3 and fixed N-C ratio of 6.625 applied when converting from mass to volumetric unit, i.e. mol kg-1 to mol m-3. Extractions for individual grid cells of the vertically integrated data set are available in ASCII format for regional models (see **Table 1**).

850

4 Direct human forcings

4.1 Population data
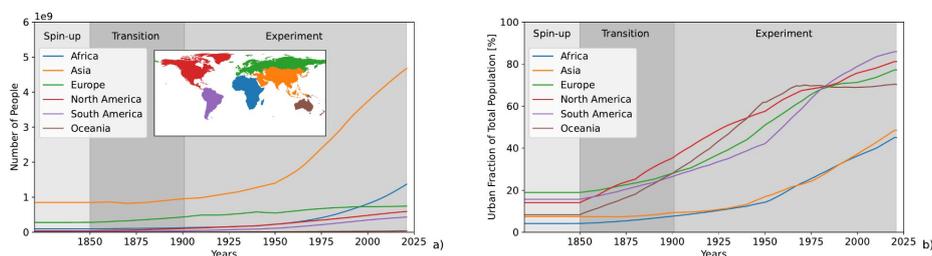
855 **Figure 4: Historical evaluation of population for different continents.** Total number of people living in the region (panel a) and urban population as a fraction of the total population per region (panel b).

Table 9: Population data provided as part of the ISIMIP3a direct human forcing.

Variable	Variable specifier	Unit	Resolution	Datasets
National population	**pop**	Number of people in millions	annual	UN 2019 WPP database (2023): census-based from 1950 to 2020 + "medium-variant" forecast provided for 2021
Gridded total population	**total-population**	Number of people	0.5°x 0.5°, annual	HYDE3.3 data for 1950-2020 constantly extended to 2021 and adjusted to match the national UN numbers described above (see text below)
Gridded rural population	**rural-population**	Number of people	0.5°x 0.5°, annual	HYDE3.3 data for 1950-2020 constantly extended to 2021 and rescaled by the same national scaling factors as the total population
Gridded urban population	**urban-population**	Number of people	0.5°x 0.5°, annual	HYDE3.3 data for 1950-2020 constantly extended to 2021 and rescaled by the same national scaling factors as the total population

860

National data. Annual national population data are taken from the 2019 UN World Population Prospects (WPP) database for the period from 1950 – 2021 (United Nations, 2019). The 2019 revision of the WPP provides census-based population numbers from 1950 through 2020. For the year 2021, we use the "medium-variant" of the probabilistic forecast also provided by the WPP. The forecast accounts the

865   past experience of each country, while reflecting uncertainty about future changes based on the past experience of other countries under similar conditions (see United Nations, 2019 for details). For countries not covered in the database, estimates are taken from the MissingIslands dataset (Arujo et al., 2021) to finally provide population data for 249 countries.

870   **Gridded data.** We provide gridded population data that is based on HYDE v3.3 (Klein Goldewijk, 2022). Just like the original dataset we provide total, rural and urban population per grid cell. The original HYDE 3.3 data was on a 1/12°×1/12° grid and has been interpolated to ISIMIP's 0.5°×0.5° grid. Furthermore, the land-sea distinction was modified to comply with the ISIMIP country mask (see **Table 1**). Before the year 2000 HYDE provides data every ten years, the intermediate years have been filled by linear

875   interpolation. Also, the original HYDE data ends in 2020. So to cover the whole ISIMIP3a time frame the final year 2020 has been duplicated as 2021. In this way annual coverage of 1850 to 2021 has been achieved.

All grid cells of a country, as defined by the ISIMIP fractional country map (see Table 1), have been rescaled such that the country's total population matches the numbers provided in the national

880   population data. Since the national data only starts in 1950, all years prior to 1950 have been rescaled by the national scaling factors of 1950. The urban and rural populations have been rescaled by the same national scaling factors as the total population.

885   **4.2 Gross Domestic Product (GDP)**
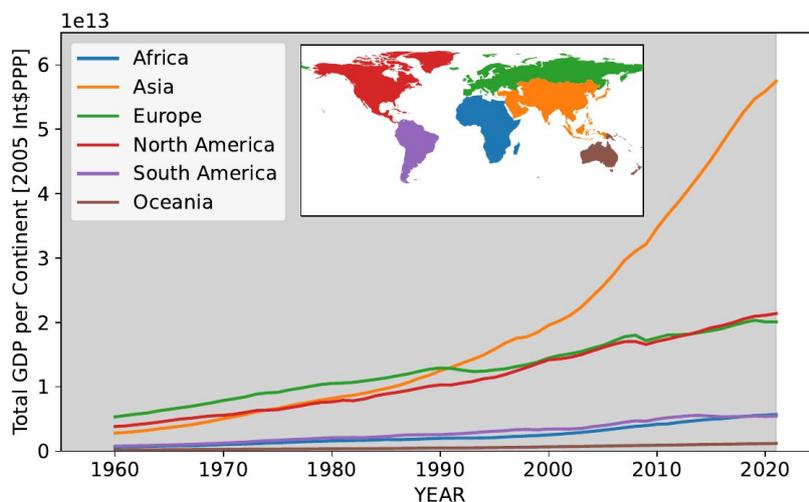
Figure 5: Aggregated GDP (Int$ PPP 2005) for different continents.

890   **Table 10: GDP data provided as part of the ISIMIP3a direct human forcing.**

Variable	Variable specifier	Unit	Resolution	Datasets
National Gross Domestic Product	**gdp**	Int$ PPP 2005	annual	World Bank's World Development Indicator database (Anon, 2008)
Gridded Gross Domestic Product	**gridded-gdp**	Int$ PPP 2005	annual	National GDP data downscaled to the 0.5° grid according to Wang and Sun, 2022

National GDP data. Time series of per-capita GDP for the time period 1960-2021 are taken from the World Bank's World Development Indicator database (Anon, 2008) and converted into constant 2005 Int$PPP, using deflators and PPP conversion factors from WDI. For countries not covered in the WDI

895   database, data from the MissingIslands dataset (Arujo et al., 2021) is used to allow covering 249 countries. Following a method developed by Koch and Leimbach, 2023; the values for the year 2021 are derived from the IMF's World Economic Outlook short-term estimates of GDP per capita growth (International Monetary Fund, 2021) that comprise estimates of the growth impacts of the Covid-19 shock.

900

Gridded GDP data. Gridded GDP data at 0.5 degree resolution are derived from the national GDP time series by applying the LitPop method (Zhao et al., 2017; Eberenz et al., 2019), which uses gridded population and nighttime light (NTL) data to downscale national GDP data. For the GDP data provided here (Wang and Sun, 2022), the LitPop approach was applied using a combination of Hyde3.3-based

905   gridded population data and NTL images from both the NOAA's DMSP-OLS stale light database, version 4 (Earth observation group - defense meteorological satellite progam, Boulder) and the Suomi-NPP-VIIRS Day/Night Band (DNB, Elvidge et al., 2017). The Suomi-NPP-VIIRS data set is a newer product that has a higher resolution of 15 arcseconds and features a wider radiometric detection range but it was launched only in 2012. Using relations from the overlapping years allowed for improvements

910   of the longer running DMSP-OLS data. This way NTL data covering the years 2000-2020 was obtained. For the earlier years from 1960 to 1999 the NTL data from 2000 was used, and in the same vein 2021 NTL data was assumed to be identical to the 2020 values. Together with the Hyde3.3-based gridded population data provided within ISIMIP3a, the annual time series of national GDP over 1960 - 2021 were disaggregated to the ISIMIP 0.5°×0.5° grid using the LitPop approach.

915

As the disaggregation of GDP is not only based on population but also uses the NTL GDP per capita, it is not constant within different countries. Deriving the gridded GDP data from the gridded population data provided within ISIMIP3a ensures that the both data sets can be combined such that the associated GDP per capita does no longer show the artefacts that have been found in the ISIMIP2a GDP per capita

920   (ISIMIP2a: Inconsistencies between ISIMIP2 gridded GDP and gridded population data , 2023).

4.3 Land use and irrigation patterns
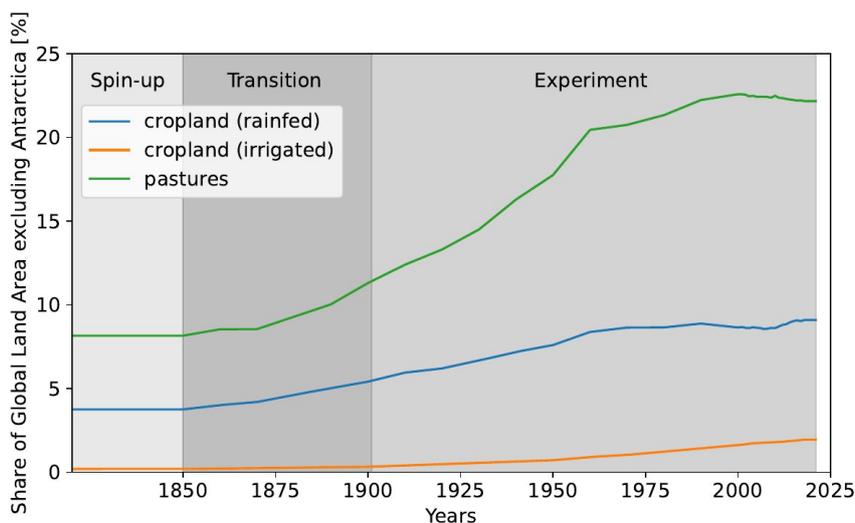
925

Figure 6: Share of Global Land Area excluding Antarctica covered by rainfed cropland (green), irrigated cropland (blue), and pasture (orange) [%]. The information is from the LUH2 data set provided as direct human forcing for ISIMIP3a (see details below).
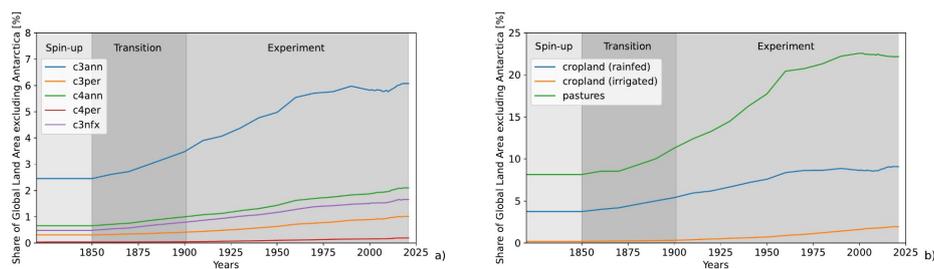
930

Figure 7: Panel A: Share of Global Land Area excluding Antarctica covered by different groups of crops (C3 annual (blue), C3 perennial (orange), C4 annual (green), C4 perennial (red, C3 nitrogen fixing (purple)). Panel B: Ratio of irrigated to rainfed land for the different groups of crops. The information is from the LUH2 data set provided as direct human forcing for ISIMIP3a (see details below).

935

Table 11: Historical land use and irrigation patterns provided as part of the ISIMIP3a direct human forcing.

Variable	Variable specifier	Unit	Resolution	Datasets
Total crop land, rainfed cropland, irrigated cropland,	**cropland_total, cropland_rainfed, cropland_irrigated, pastures**	unitless (share of area in a grid cell)	0.5°×0.5°, annual	LUH2 (Hurtt et al., 2020)

pastures				
C3 annual rainfed cropland, C3 annual irrigated cropland, C3 perennial cropland, C3 perennial, irrigated cropland, C4 annual rainfed cropland, C4 annual irrigated cropland, C4 perennial rainfed cropland, C4 perennial irrigated cropland, C3 nitrogen fixing rainfed, cropland, C3 nitrogen fixing irrigated cropland	**c3ann_irrigated, c3ann_rainfed, c3nfx_irrigated, c3nfx_rainfed, c3per_irrigated, c3per_rainfed, c4ann_irrigated, c4ann_rainfed, c4per_irrigated, c4per_rainfed**	1 (share of area in a grid cell)	0.5°×0.5°, annual	LUH2

| Cropland downscaled to 15 crops, for both rainfed and irrigated land | c3per_irrigated, c3per_rainfed, c4per_irrigated, c4per_rainfed, maize_irrigated, maize_rainfed, oil_crops_groundnut_irrigated, oil_crops_groundnut_rainfed, oil_crops_rapeseed_irrigated, oil_crops_rapeseed_rainfed, oil_crops_soybean_irrigated, oil_crops_soybean_rainfed, oil_crops_sunflower_irrigated, oil_crops_sunflower_rainfed, others_c3ann_irrigated, others_c3ann_rainfed, others_c3nfx_irrigated, others_c3nfx_rainfed, pulses_irrigated, pulses_rainfed, rice_irrigated, rice_rainfed, temperate_cereals_irrigated, temperate_cereals_rainfed, temperate_roots_irrigated, temperate_roots_rainfed, tropical_cereals_irrigated, tropical_cereals_rainfed, tropical_roots_irrigated, tropical_roots_rainfed | 1 (share of area in a grid cell) | 0.5°×0.5° annual | downscaling of LUH2 data based on the crop distribution from Monfreda et al., 2008. The method is described in Frieler et al., 2017

The 5 LUH2 crop types are split up into the following sub categories:

C3 annual disaggregated: rapeseed, rice, temperate cereals, temperate roots, tropical roots, sunflower, others C3 annual

C3 perennial: (no further disaggregation)

C3 nitrogen-fixing: groundnut, pulses, soybean, others C3 nitrogen-fixing

C4 annual: maize, tropical cereals

C4 perennial: sugarcane |

Managed pastures, rangeland	**Managed_pastures, rangeland**	1 (share of area in a grid cell)	0.5°×0.5°, annual	LUH2

Historical land use and irrigation patterns for ISIMIP3a and ISIMIP3b, group I and group II simulations
are taken from LUH2 (Hurtt et al., 2020). The data set is, up to 2018, identical to the data provided with
ISIMIP2b. The data are based on the HYDE 3.2 land use data set (Klein Goldewijk et al., 2017) and
have been constantly extended up to 2021, i.e., by copying the 2018 patterns into 2019, 2020, and
2021.

The original HYDE 3.2 data distinguishes four categories of land use: rainfed and irrigated cropland,
managed pastures, and more extensively managed rangelands (see **Table 11**). The latter two
categories are combined to grazing lands (ISIMIP variable 'pastures').

In LUH2 the crop land information is further downscaled to five crop types: C3 annual plants, C3
perennial plants, C3 nitrogen fixing plants, C4 annual plants and C4 perennial plants. In the same vein
as the HYDE case, the LUH2 data set distinguishes between rainfed and irrigated croplands.

For the purpose of driving the ISIMIP impact models, the LUH2 data was interpolated from the original
0.25° × 0.25° to the standard ISIMIP 0.5° × 0.5° global grid.

In a further downscaling step the 5 crops land use data has been downscaled even further to 15 crop
types. For this purpose the Monfreda land use dataset (Monfreda et al., 2008) has been used. It
describes the crop land areas of 175 crops in the year 2000, and we use this to downscale the 5 crops
categories into land use areas of 15 more specific crop types (maize, groundnut, rapeseed, soybeans,
sunflower, rice, sugarcane, pulses, temperate cereals (including wheat), temperate roots, tropical
cereals, tropical roots, others annual, others perennial, and others N-fixing). The ratios determined from
the year 2000 numbers have then been applied to all years. For further details please refer to Frieler et
al., 2017.

4.4 Fertiliser input
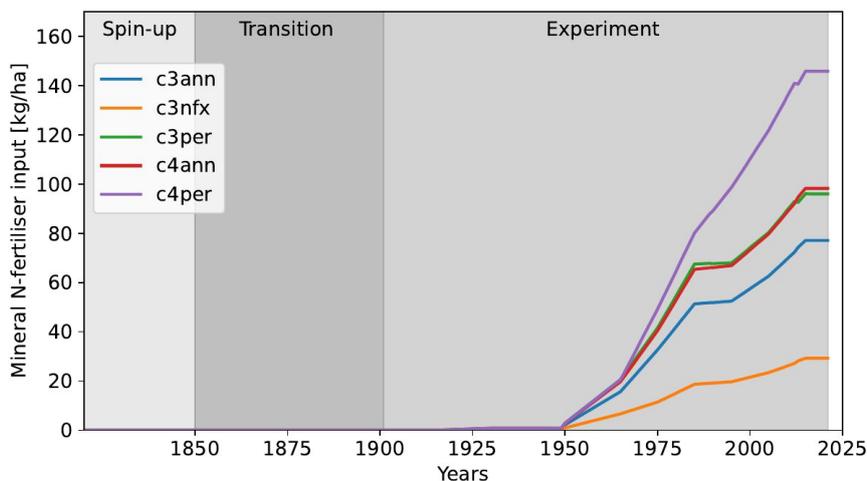
Figure 8: Mean mineral N-fertiliser input averaged across the land areas where the considered crop groups are grown.

970

Table 12: Fertiliser inputs provided as part of the ISIMIP3a direct human forcing.

Variable	Variable specifier	Unit	Resolution	Datasets
Mineral N-fertiliser for 5 crop types (C3 annual, C3 perennial, C4annual, C4 perennial, C3 nitrogen fixing)	**fertl_c3ann, fertl_c3per, fertl_c4ann, fertl_c4per, fertl_c3nfx**	kg ha-1 yr-1 (crop season)	0.5°×0.5°, annual	LUH2

The LUH2 data set also includes national application rates of industrial nitrogen fertiliser (Hurtt et al.,
975   2020). This does not include manure. The fertiliser data is not based on HYDE but was derived from
other sources. The data for the years 1915–1960 are based on (Smil, 2001), 1961–2011 are based on
a compilation by Zhang et al., 2015 which in turn is based on FAOSTAT (FAO, 2016), and 2012–2015
are based on a projection by the International Fertilizer Association (IFASTAT, 2015). For the pure crop
runs within ISIMIP, where the considered crops are assumed to to be grown everywhere without a land
980   use specification, the LUH2 national fertiliser inputs are assumed to be applied everywhere within the
country.

4.5 Land transformation

985   **Table 13: Land transformation and wood harvest provided as part of the ISIMIP3a direct human forcing.**

Variable	Variable specifier	Unit	Resolution	Datasets
Wood harvest	**primf-harv** (wood harvest area from primary forest land) **primn-harv** (wood harvest area from primary non-forest land) **secmf-harv** (wood harvest area from secondary mature forest land) **secyf-harv** (wood harvest area from secondary young forest land) **secnf-harv** (wood harvest area from secondary non-forest land) **primf-bioh** (wood harvest biomass carbon from primary forest land) **primn-bioh** (wood harvest biomass carbon from primary non-forest land) **secmf-bioh** (wood harvest biomass carbon from secondary mature forest land) **secyf-bioh** (wood harvest biomass carbon from secondary young forest land) **secnf-bioh** (wood harvest	Fraction of the national land area, kg in case of biomass	Annual, national sum	Based on LUH2 v2h (Hurtt et al., 2011, 2020; del Valle et al., 2022)

	biomass carbon from secondary non-forest land)			
Not forest-related land transformation All transitions from one type of land use to another	**<>_to_<>** Considered land types: **secdf** (potentially forested secondary land), **secdn** (potentially non-forested secondary land), **urban** (urban land), **c3ann** (C3 annual crops), **c4ann** (C4 annual crops), **c3per** (C3 perennial crops), **c4per** (C4 perennial crops), **c3nfx** (C3 nitrogen-fixing crops), **pastr** (managed pasture) **range** (rangeland)	Fraction of the grid cell	Annual	Based on LUH2 v2h (Hurtt et al., 2011, 2020)

These datasets are based on the LUH v2h Harmonization Data Set covering 850 to 2015 (Hurtt et al., 2020). The wood harvest data were obtained by aggregating from the original LUH2 grid to the ISIMIP 0.5° × 0.5° grid (first-order conservative remapping) and then aggregating to the national sums. Wood

990   harvesting data are used in the vegetation models to mimic wood removal as part of forest management and clearing, and has a strong influence on the carbon balance. National data are provided so that models can use their internal routines to distribute the harvesting within a country's forest area. The gridded land transformation data were obtained by aggregating from the original LUH2 grid to the ISIMIP 0.5° × 0.5° grid; these data always end a year earlier than all other land use data, because a

995   year in these data sets actually describes the changes from the current to the next year. The data have been extended up to 2021 by copying the 2015 data into the following years (files end in 2020).

4.6 Nitrogen Deposition

1000

Table 14: Nitrogen deposition provided as part of the ISIMIP3a direct human forcing.

Variable	Variable specifier	Unit	Resolution	Datasets
Reduced nitrogen deposition	**nhx**	g N m-2 mon-1	monthly	based on simulations from Tian et al., 2018
Oxidised nitrogen deposition	**noy**	g N m-2 mon-1	monthly	based on simulations from Tian et al., 2018

1005 Reduced and oxidised nitrogen deposition (NHx, NOy) are based on simulations by the NCAR Chemistry-Climate Model Initiative during 1850-2014 (Tian et al., 2018). Nitrogen deposition data was interpolated to 0.5° by 0.5° using the nearest grid point method. Data in 2015-2021 are assumed to be the same as that in 2014.

4.7 Crop calendar

1010

Table 15: Crop calendar provided as optional representation of agricultural management

Variable	Variable specifier	Unit	Resolution	Datasets
Planting day, separated for rainfed and irrigated crops where applicable	**planting_day**	day of year	0.5°, time average, no variation in time	Jägermeyr et al., 2021b
Maturity day, separated for rainfed and irrigated crops where	**maturity_day**	day of year	0.5°, time average, no variation in time	Jägermeyr et al., 2021b

applicable				

Unfortunately, there is no global data set describing changes in growing seasons across the historical period. Instead we provide a static crop calendar that has been developed within the AgMIP Global Gridded Crop Model Intercomparison GGCMI and merges information from various observational data sources (Jägermeyr et al., 2021b). It provides planting and maturity days for 18 different crops at the ISIMIP standard 0.5° grid. Grid cells outside of currently cultivated areas are spatially extrapolated (details below). For wheat and rice two growing seasons are provided while for all other crops the calendar only specifies one main growing season. The reported growing seasons should not be considered the growing seasons for one specific year but as 'representative growing season' across the recent years. Within the crop models different crop varieties are represented by the heat units required to reach physiological maturity. The crop calendar should be implemented by adjusting the required heat units to the average of the annual sums of heat units between the specified planting and maturity date over all growing seasons between 1979 and 2010.

If modellers use a temporal adjustment of cultivars by varying required heat units in response to socio-economic development or historical climate change this is certainly allowed within the 'histsoc' set-up. If cultivars are fixed according to the method described above this simulation will be considered a '2015soc' simulation as long as other direct human drivers are also held constant at 2015 levels. However, if, e.g., fertiliser inputs are varied over time according to provided forcing data (see section **4.4**), the run will be considered a 'histsoc' run.

GGCMI is currently working on a temporally resolved global crop calendar at the same spatial resolution based on various new data sources including agricultural ministries, census reports, phenological data bases, experimental sites, etc. This data set will be published separately and could then be used to inform 'histsoc' simulations.

4.8 Dams and reservoirs

Table 16: Information about dams and reservoirs

Variable	Variable specifier	Unit	Resolution	Datasets
Unique ID for each point representing a dam and its associated reservoir.	ID	unitless numbers: 1-7320 from GRanD and	per dam	Global Reservoir and Dam Database (GRanDv1.3,

		J3-J26 from GeoDAR v1.2		data up to 2016; Lehner et al., 2011a, b) and GeoDAR v1.2 (Wang et al., 2022) covering the period 2016-2020
Name of the dam structure	**DAM_NAME**	unitless	per dam	GRanDv1.3, GeoDARv1.2
Original longitudinal location of the dam	**LON_ORIG**	degree (°)	per dam	GRanDv1.3, GeoDARv1.2
Original longitudinal location of the dam	**LAT_ORIG**	degree (°)	per dam	GRanDv1.3, GeoDARv1.2
Longitude, adjusted to the ISIMIPddm30 0.5° grid cell centres	**LON_DDM30**	degree (°)	per dam	Adjustment of original GRanDv1.3, GeoDARv1.2 data
Latitude, adjusted to the ISIMIPddm30 0.5° grid cell centres	**LAT_DDM30**	degree (°)	per dam	Adjustment of original GRanDv1.3, GeoDARv1.2 data
Upstream area draining into the reservoir using ISIMIPddm30	**CATCH_SKM_DDM30**	km²	per dam	Derived from dam location and the ISIMIPddm30 drainage map.
Upstream area draining into the reservoir acc. to GRanD [km²]	**CATCH_SKM_GRanD**	km²	per dam	GRanDv1.3
Representative maximum storage	**CAP_MCM**	10^6 m³	per dam	GRanDv1.3, GeoDARv1.2

capacity of reservoir				
Year of construction, completion, commissioning, etc. (not specified)	**YEAR**	year	per dam	GRanDv1.3, GeoDARv1.2 + complemented by internet research
Alternative year (may indicate multi-year construction, secondary dam, etc.)	**ALT_YEAR**	year	per dam	GRanD
Original, rounded location has been shifted with automatic mapping (FLAG_CORR=1) If visual check or manual re-location has been applied (FLAG_CORR=2)	**FLAG_CORR**	Unitless labels: 1 or 2	per dam	Introduced when adjusting the locations to the ISIMIPddm30 0.5° grid
Name of the river which the dam impounds	**RIVER**	unitless	per dam	GeoDARv1.2. For GRanD records, it can be found in the GRanD database
Country where the dam is located	**COUNTRY**	unitless	per dam	GeoDARv1.2. For GRanD records, it can be found in the GRanD database
Height of the dam. If multiple heights are available, the	**D_Hght_m**	m	per dam	GeoDARv1.2. For GRanD records, it can be found in the

foundation height was used.				GRanD database
Maximum inundation area of the reservoir	**R_Area_km2**	km²	per dam	GeoDARv1.2. For GRanD records, it can be found in the GRanD database
Maximum inundation length of the reservoir	**R_Lgth_km**	km	per dam	GeoDARv1.2. For GRanD records, it can be found in the GRanD database
Main purpose(s) of the dam	**PURPOSE**	no units	per dam	GeoDARv1.2. For GRanD records, it can be found in the GRanD database
Sources used to collect this dam's information	**SOURCE**	no units	per dam	GeoDARv1.2. For GRanD records, it can be found in the GRanD database. If filled out for GeoDAR records, it corresponds to the source for the year of construction/

				commissioning
Other notes related to the mapping or re-location of dams to ISIMIPddm30	**COMMENTS**	no units	per dam	

1040 In order to offer a consistent and common source of information about reservoirs and associated dams for climate impact modellers (see **Table 16**), we joined the Global Reservoir and Dam Database of the Global Water System Project (GRanD v1.3; Lehner et al., 2011a, b) with a subset of the Georeferenced global Dams And Reservoirs (GeoDAR v1.2) database (Wang et al., 2022), developed at Kansas State University (KSU), and provided by Jida Wang ahead of publication. These additional dams have

1045 construction or projected finalisation dates between 2016 and 2025, while GRanD v1.3 includes dams constructed up until 2017. In total, the combined database now includes 7331 dams whose construction was finished by 2025. It includes dams that were constructed before, but still in existence during, the simulation period (the first reported dam was finished in the year 286). In total the reported dams have a global cumulative storage capacity of approximately 6932 km^3 (**Figure 2**). For the simulations

1050 described here, dams with (projected) construction dates after 2020 are not considered; these will become relevant in the ISIMIP3b group III simulations, with exception of the Grand Ethiopian Renaissance Dam, which we decided to include since its reservoir reached a first stage of filling of 4.9 km^3 in July 2020 (BBC news: Nile dam row, 2020; Tractebel: Filling of the reservoir of the Grand Renaissance Dam, 2020).

1055
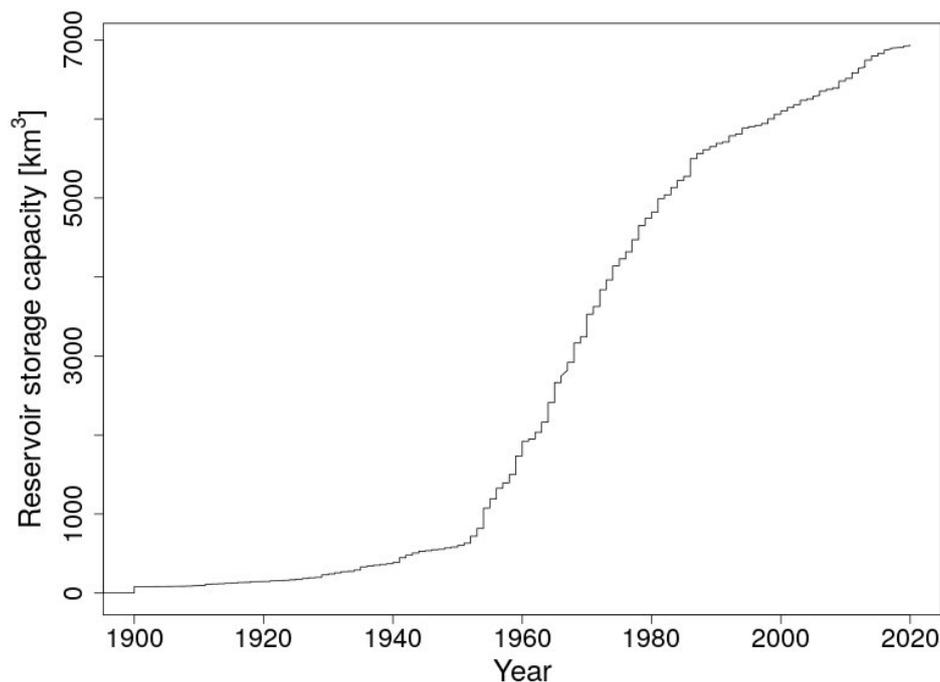
Figure 9: Cumulative reservoir storage capacity between 1900 and 2020. Reservoirs that are active before the year 1901 have been assigned to the year 1900. Horizontal axis shows year of construction, completion, or commissioning, reflecting ambiguity in available data.

1060

The original GRanDv1.3 dam locations were mapped to the global 30-min drainage direction map (ISIMIPddm30, Müller Schmied, 2022) based on DDM30 (Döll and Lehner, 2002), by applying the following algorithm:

Firstly, the locations have been rounded to the closest 0.5° grid cell centre. Then, the area of the

1065 upstream catchment draining into the GRanD reservoirs (previous version of GRanDv1.3) in the ISIMIPddm30 map have been calculated and compared against the ones reported in GRanD. All dams with an upstream area bigger than 10000 km² in GRanD and more than 50% deviation from the GRanD upstream area have been shifted to the 8 possible neighbouring cells. If any of these shifts resulted in a smaller deviation from the GRanD upstream areas, the dam was moved to the grid cell resulting in

1070 the smallest deviation in the upstream area.

Additionally, a visual validation and, where appropriate, manual relocation were applied with the aim to find the best fitting grid cell from a hydrological perspective. Due to the grid cell resolution, reservoirs might get assigned to a grid cell that include the main stream or already a confluence of one or more tributaries even though the dam is located in a particular tributary according to the database. In those

1075 cases, and based on visual GIS inspection, the best location was searched, e.g. by moving the dam location one cell upstream to preserve the routing order and to avoid a different or much deviating river basin in the ISIMIPddm30 stream network. In case a dam is not assigned to any river basin in the ISIMIPddm30 (which can happen due to the difference in spatial resolution), the most suited location

according to the observed upstream area was selected. Because of limited capacity, this visual
validation procedure was applied only for dams present in the earlier GranDv1.1 version that have a
maximum storage capacity greater than 0.5 km³ (1108 dams), as well as for all the 458 additional dams
in GRanDv1.3 and the 11 dams (excluding post-2020 dams) added from GeoDAR v1.2, and not for
several thousand smaller dams present in GranDv1.1.

4.9 Fishing intensities
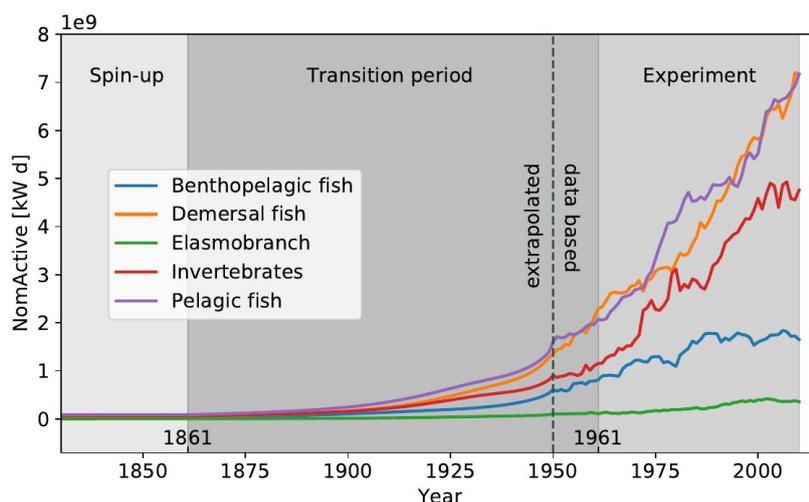
Figure 10: Evolution of historical nominal active fishing effort (NomActive) as provided for the spin-up,
transition period, and 'obsclim + histoc, default' ISIMIP3a experiment, separated by target functional group. The
groups represent an aggregation of 29 even finer categories covered by the data set (see **Table 17**).

Table 17: Information about historical fishing intensities provided as DHF within ISIMIP3a. For the spin-up
+ transition period required by models within the *marine ecosystems and fisheries* sector the forcing is provided
for 1841-2010 although the 'obsclim + histoc, default' experiment only starts in 1961.

Variable	Variable specifier	Unit	Resolution	Datasets
Total nominal active fishing effort (i.e., accounting for total power of the fleet but not including changes in the efficiency of fishing technology) separated by fishing sector, fleet, and target functional groups.	**NomActive**	kW d (kilowatts of fleet power times days at sea)	annual data spatially grouped by Exclusive Economic Zones (EEZ), assigned to fishing country codes from the Sea Around Us Project (SAUP), and nested within Large Marine Ecosystems. Masks	Reconstruction based on historical yearbook and FAO compilations (Rousseau et al., 2022 based on Rousseau et al., submitted 2023). The reconstructions have been extended

			for the latter are provided as static geographic information (see **Table 1**).	backwards to 1841 by constant 1861 values to cover the 120 years of spin-up required for the marine ecosystems and fisheries models

1095 The data set of reconstructed historical fishing efforts (Rousseau et al., 2022) serves as the DHF for the *marine ecosystems and fisheries* sector. The efforts are quantified for 'artisanal' and 'industrial' fishing (sector), 66 Large Marine Ecosystems (LME), 187 national Exclusive Economic Zones (EEZ) and 'high seas', 244 country identifiers from the Sea Around Us Project (SAUP), 16 different categories of applied gears (e.g. bottom trawls, longlines and purse seines), 29 target functional groups,

1100 separately.

The original annual time series spanning 1950-2015 were further extrapolated into the past to 1861 using generalised additive models (Rousseau et al., submitted 2023; see Figure 10). To cover the 'spin-up + transition' period from 1841-1960 the data set has been extended backwards by 1861 values. Forcing with this dataset allows for a comparison of simulated catches against the congruent (Watson,

1105 2019) reconstruction of historical fisheries catches (spanning the period 1869-2015; Watson and Tidd, 2018). To permit integration into marine ecosystem models that capture different fishing sectors, fleets, and functional groups these data include nominal active fishing effort disaggregated by location (Exclusive Economic Zone/High Seas and Large Marine Ecosystem), fishing country, fishing gear, targeted functional group, and fishing sector (coastal artisanal and industrial). Impact modellers are

1110 allowed to distribute this effort across space, time, and target organisms in any method compatible with their models' structure. The fishing effort data does not include any information about changes in the efficiency of fishing technology over time (technological creep). Assumptions about these efficiencies are left to the individual modellers and usually determined in model calibration.

1115 **4.10 Forest management for *regional forest* sector**

Table 18: Information about historical forest management provided as DHF for the *regional forest* sector within ISIMIP3a

Variable	Variable specifier	Unit	Resolution	Datasets
Silvicultural system	**sysi**	na	stand	Reyer et al., 2023
Tree species	**species**	na	stand	Reyer et al., 2023

Harvest type	**harvtype**	na	stand	Reyer et al., 2023
Thinning type	**thintype**	% of basal area	stand	Reyer et al., 2023
Rotation length	**rotlength**	year	stand	Reyer et al., 2023
Thinning frequency	**thinfrequ**	year	stand	Reyer et al., 2023
Year of Management intervention	**manyear**	year	stand	Reyer et al., 2023
Type of management intervention	**mantype**	na	stand	Reyer et al., 2023
Regeneration species	**regen**	na	stand	Reyer et al., 2023
Planting density	**plantdens**	na	stand	Reyer et al., 2023
Planting age	**plantage**	year	stand	Reyer et al., 2023
Planting seedling height	**planthei**	m	stand	Reyer et al., 2023
Planting diameter at breast height	**plantdbh**	cm	stand	Reyer et al., 2023
Age when diameter at breast height is reached	**dbhage**	year	stand	Reyer et al., 2023
Stem number	**stemno**	na	stand	Reyer et al., 2020a based on Reyer et al., 2020b

1120   For the *regional forest* sector, forest management is defined for nine forest sites in Europe, four in Germany (Peitz, KROOF, Solling-beech, Solling-spruce) as well in Czech Republic (Bily Kriz), Denmark

(Sorø), France (Le Bray), Italy (Collelongo) and Finland (Hyytiälä) (Reyer et al., 2020b). For the
historical period, observed stem numbers and forest thinning types are provided in the same ways as
in ISIMIP2b from the PROFOUND Database (Reyer et al., 2020b) so that modellers can mimic the
1125 exact management that has happened at the site and perform the histsoc runs as close to reality as
possible. Additionally, a set of forest site-specific forest management rules and planting numbers based
on historical standard management practices of the area where the forest sites are located are defined
and spelled out in concrete management schedules to enable modellers to simulate '2015soc'
conditions (Reyer et al., 2023).

1130

5 Discussion

This paper aims to give an overview over the ISIMIP3a experiments and the provided climate-related
and direct human forcing data sets. It is intended to work as a catalogue where modellers can find all
1135 relevant information about the data sets they need as reference for the impact model simulations within
ISIMIP3a. As a community-driven initiative across multiple disciplines the selection of the best available
forcing data for ISIMIP builds on the expertise within the different sectoral communities.
We would like to improve or complement these data sets in a continuous process wherever possible.
So this paper can also be read as a call for contributing additional data that could i) either be provided
1140 optionally within the current round as the optional data sets do not have to be harmonised across all
model simulations or ii) as mandatory forcing for an upcoming simulation round. In particular, we aim
for temporally resolved historical growing seasons that have been shown to be critical to reproduce
observed crop yields (Jägermeyr and Frieler, 2018), counterfactual oceanic climate-related forcings,
counterfactual TC-related precipitation (Risser and Wehner, 2017; van Oldenborgh et al., 2017; Wang
1145 et al., 2018; Patricola and Wehner, 2018), temporally resolved lightning data for the full set of considered
climate model simulations, and temporally resolved human drainage and restoration activities in
peatlands as one of the key controls over global peatland greenhouse gas emissions (Loisel et al.,
2020).
We believe that the ISIMIP3a framework will significantly move forward our understanding of observed
1150 changes in natural and human systems and their respective drivers. As impact models encode our
process knowledge on how several drivers (climate-related ones as well as direct human influences)
come together to generate observed changes, they are ideal tools for this task. The ISIMIP3a evaluation
experiments will help to clarify how well the current generation of impact models can explain observed
changes in impacted systems based on provided information about the different forcings. High
1155 explanatory power then allows for impact attribution through the ISIMIP3a attribution experiments
following the IPCC-WGII definition of AR6, disentangling changes in climate-related forcings from other
drivers of change. The setup is the first that allows to easily and broadly address impact attribution
across many impact categories. This will fill an important gap as only few process-based impact models
have been used in this field despite their general suitability. The here presented work can thus lay the
1160 ground for urgently necessary works to inform climate litigation, the loss and damage debate, and last
but not least also decisions about short term adaptation measures. It will ultimately help to carve out

the sensitivity of our ecosystems and human societies to historical climate change, which is a precondition for robustly projecting future climate impacts.

1165 **Author contribution:** KF lead the project and developed the concept with contributions from JS, MM, CO, CPOR, JLB, CSH, CMP, TDE, KOC, CN, RH, DT, OM, JJ, GL, SC, EB, AGS, NS, JC, SH, CB, AG, FL, SNG, HMS, FH, TH, RM, DP, WT, DMB, MB. JV supported the data generation. SL provided atmospheric climate forcing data. MM provided coastal water level data and atmospheric forcing data. MdRRL, JW and FY provided dam data. CO and IJS provided GDP data. CPOR provided forest

1170 management data. DNK and JTM provided high resolution climate forcing data. ST provided coastal water levels and counterfactual climate forcing data. YR provided data on fishing efforts. CS and XL provided ocean forcing data. TV provided TC data. TW and FS provided gridded GDP data. IV provided lake data. JJ provided growing seasons. CM provided soil data. KF prepared the manuscript with contributions from all co-authors.

1175

Code and data availability: All input data described is available for participating modelers with a respective account at the DKRZ server. Data will be made publicly available, and most data is already publicly available at https://data.isimip.org/. Availability is documented on www.isimip.org where the way of accessing the data is described, as well. Model output is already partly available at

1180 https://data.isimip.org/.

The ISIMIP Repository fulfills the Archive standards as stated in the "GMD code and data policy". The Repository is hosted and maintained by the Potsdam Institute for Climate Impact Research (PIK). Data can only be published or removed from the repository by the ISIMIP data team, that is monitored by the ISIMIP steering committee according to the organisational structure of ISIMIP (ISIMIP organigram,

1185 2020). DOI are used to refer to datasets in a persistent way. Whenever a dataset is replaced for any reason a copy is kept on tape, and a new DOI is issued, while the old DOI is kept online with information on how to retrieve the archived data. Detailed information can be found in the ISIMIP terms of use (ISIMIP terms of use, 2022).

1190 **Competing interests:** At least one of the (co-)authors is a member of the editorial board of Geoscientific Model Development.

Acknowledgements

This article is based upon work from COST Action CA19139 PROCLIAS (PROcess-based models for

1195 CLimate Impact Attribution across Sectors), supported by COST (European Cooperation in Science and Technology; https://www.cost.eu). Funding from the EU Horizon 2020 research and innovation program under grant agreement 821010 (CASCADES) supported the work of C.P.O.R., J.V. and I.D.VdV., and the provisioning of the high resolution climate data, and supported the work of ST under grant agreement No 820712 (RECEIPT). SL received funding from the German Research Foundation

1200 (DFG, project number 427397136). The German Federal Ministry Ministry of Education and Research (BMBF) supported the work under the research projects ISIAccess (16QK05), SLICE (01LA1829A),

QUIDIC (01LP1907A), CHIPS (01LS1904A), ISIpedia (01LS1711A). FL received funding from the National Key Research and Development Program of China (project number 2022YFE0106500). JC received funding from the National Key Research and Development Program of China (project number 2022YFF0801904). MB acknowledges funding from the Research Foundation—Flanders (FWO, G095720N). SC and NS were supported by the National Environmental Research Council (NERC) grant NE/R015791/1. SC, AGS, MB and NS acknowledge funding through NERC NE/V01854X/1 (MOTHERSHIP). CB was supported by the Newton Fund through the Met Office. The research by DNK was funded through the 2019-2020 BiodivERsA joint call for research proposals, under the BiodivClim ERA-Net COFUND program, and with the funding organisations Swiss National Science Foundation SNF (project: FeedBaCks, 193907), and the Swiss National Science Foundation SNF (project: Adohris, 205530). RM was supported by the Alter-C project (PID2020-114024GB-C32/AEI /10.13039/501100011033). CSH was supported by Open Philanthropy, NSF award 2218777, and NOAA CPO.

1215 **References**

BBC news: Nile dam row, 2020: https://www.bbc.com/news/world-africa-53573154; July 2020, last access: 10 February 2023.

ISIMIP2a: Inconsistencies between ISIMIP2 gridded GDP and gridded population data:
1220 https://data.isimip.org/caveats/4/, last access: 10 February 2023.

Earth observation group - defense meteorological satellite progam, boulder:
https://www.ngdc.noaa.gov/eog/dmsp/downloadV4composites.html, last access 15 February 2023.

WOCE Atlas: http://woceatlas.ucsd.edu , last access: 11 January 2023.

Sea Around Us Area Parameters and Definitions: https://www.seaaroundus.org/sea-around-us-area-
1225 parameters-and-definitions/, last access 15 February 2023.

International Monetary Fund: World economic outlook, 2021, last access 15 February 2023.

GSWP3 documentation: http://hydro.iis.u-tokyo.ac.jp/GSWP3/, last access: 9 January 2023.

GSWP3 soil texture map: http://hydro.iis.u-tokyo.ac.jp/~sujan/research/gswp3/soil-texture-map.html,
upscaling method A., last access 28 April 2022
1230
GGCMI-HWSD: https://github.com/AgMIP-GGCMI/processing_hwsd_for_GGCMI, last access: 9
February 2023

Tractebel: Filling of the reservoir of the Grand Renaissance Dam: https://tractebel-
1235 engie.com/en/news/2020/ethiopia-first-stage-of-the-filling-of-the-reservoir-of-the-grand-renaissance-
dam, September 2020, last access: 10 February 2023.

UN 2019 World Population Prospects (WPP) Database 2019: https://population.un.org/wpp/, last
access: 15 February 2023

1240 Albrecht, T., Winkelmann, R., and Levermann, A.: Glacial-cycle simulations of the Antarctic Ice Sheet
with the Parallel Ice Sheet Model (PISM) – Part 2: Parameter ensemble analysis, Cryosphere, 14,
633–656, https://doi.org/10.5194/tc-14-633-2020, 2020.

Arujo, E., Bodirsky, B. L., Crawford, M. S., Leip, D., and Dietrich, J.: MissingIslands dataset for filling
in data gaps from the WDI datasets, Zenodo [data set] https://doi.org/10.5281/zenodo.4421504, 2021.

1245 Brun, P., Zimmermann, N. E., Hari, C., Pellissier, L., and Karger, D. N.: CHELSA-BIOCLIM+ A novel
set of global climate-related predictors at kilometre-resolution, EnviDat [data set],
https://doi.org/10.16904/envidat.332, 2022a.

Brun, P., Zimmermann, N. E., Hari, C., Pellissier, L., and Karger, D. N.: Global climate-related
predictors at kilometre resolution for the past and future, Earth Syst. Sci. Data, 14, 5573–5603,
1250 https://doi.org/10.5194/essd-2022-212, 2022b.

Büchner, M. and Reyer, C.: ISIMIP3a atmospheric composition input data (v1.2), ISIMIP Repository
[data set], https://doi.org/10.48364/ISIMIP.664235.2, 2022.

Caron, L., Ivins, E. R., Larour, E., Adhikari, S., Nilsson, J., and Blewitt, G.: GIA model statistics for
GRACE hydrology, cryosphere, and ocean science, Geophys. Res. Lett., 45, 2203–2212,
1255 https://doi.org/10.1002/2017gl076644, 2018.

Cecil, D.: LIS/OTD 0.5 Degree High Resolution Monthly Climatology (HRMC), NASA Global
Hydrometeorology Resource Center DAAC [data set], Huntsville, Alabama, U.S.A.,

https://doi.org/10.5067/LIS/LIS-OTD/DATA303, 2006.

1260   Chavas, D. R. and Lin, N.: A Model for the Complete Radial Structure of the Tropical Cyclone Wind Field. Part II: Wind Field Variability, J. Atmos. Sci., 73, 3093–3113, https://doi.org/10.1175/JAS-D-15-0185.1, 2016.

Compo, G. P., Whitaker, J. S., Sardeshmukh, P. D., Matsui, N., Allan, R. J., Yin, X., Gleason, B. E., Vose, R. S., Rutledge, G., Bessemoulin, P., Brönnimann, S., Brunet, M., Crouthamel, R. I., Grant, A. N., Groisman, P. Y., Jones, P. D., Kruk, M. C., Kruger, A. C., Marshall, G. J., Maugeri, M., Mok, H. Y.,
1265   Nordli, Ø., Ross, T. F., Trigo, R. M., Wang, X. L., Woodruff, S. D., and Worley, S. J.: The twentieth century reanalysis project, Quart. J. Roy. Meteor. Soc., 137, 1–28, https://doi.org/10.1002/qj.776, 2011.

Cucchi, M., Weedon, G. P., Amici, A., Bellouin, N., Lange, S., Müller Schmied, H., Hersbach, H., and Buontempo, C.: WFDE5: bias-adjusted ERA5 reanalysis data for impact studies, Earth Syst. Sci.
1270   Data, 12, 2097–2120, https://doi.org/10.5194/essd-12-2097-2020, 2020.

Dangendorf, S., Hay, C., Calafat, F. M., Marcos, M., Piecuch, C. G., Berk, K., and Jensen, J.: Persistent acceleration in global sea-level rise since the 1960s, Nat. Clim. Chang., 9, 705–710, https://doi.org/10.1038/s41558-019-0531-8, 2019.

Danielson, J. J. and Gesch, D. B.: Global multi-resolution terrain elevation data 2010 (GMTED2010),
1275   U.S. Geological Survey, https://doi.org/10.3133/ofr20111073, 2011.

Dirmeyer, P. A., Gao, X., Zhao, M., Guo, Z., Oki, T., and Hanasaki, N.: GSWP-2: Multimodel Analysis and Implications for Our Perception of the Land Surface, Bull. Am. Meteorol. Soc., 87, 1381–1398, https://doi.org/10.1175/BAMS-87-10-1381, 2006.

Malle, Johanna. 2023. w5e5_downscale. Github. https://github.com/johanna-malle/w5e5_downscale.

1280   Döll, P. and Lehner, B.: Validation of a new global 30-min drainage direction map, J. Hydrol., 258, 214–231, https://doi.org/10.1016/S0022-1694(01)00565-0, 2002.
Eberenz, S., Stocker, D., Röösli, T., and Bresch, D. N.: LitPop: Global Exposure Data for Disaster Risk Assessment, ETH Zurich [data set], http://dx.doi.org/10.3929/ETHZ-B-000331316, 2019.

Eberenz, S., Lüthi, S., and Bresch, D. N.: Regional tropical cyclone impact functions for globally
1285   consistent risk assessments, Nat. Hazards Earth Syst. Sci., 21, 393–415, https://doi.org/10.5194/nhess-21-393-2021, 2021.

Elvidge, C. D., Baugh, K., Zhizhin, M., Hsu, F. C., and Ghosh, T.: VIIRS night-time lights, Int. J. Remote Sens., 38, 5860–5879, https://doi.org/10.1080/01431161.2017.1342050, 2017.

Emanuel, K. and Rotunno, R.: Self-Stratification of Tropical Cyclone Outflow. Part I: Implications for
1290   Storm Structure, J. Atmos. Sci., 68, 2236–2249, https://doi.org/10.1175/JAS-D-10-05024.1, 2011.

Fagnant, C., Gori, A., Sebastian, A., Bedient, P. B., and Ensor, K. B.: Characterizing spatiotemporal trends in extreme precipitation in Southeast Texas, Nat. Hazards, 104, 1597–1621, https://doi.org/10.1007/s11069-020-04235-x, 2020.

FAO (Food and Agriculture Organization of the United Nations): Fertilizer data, Faostat, FAO
1295   Statistical Databases [data set], available at https://www.fao.org/faostat/en/#data/RFN/, 2016.

FAO, IIASA, ISRIC, ISSCAS, JRC: Harmonized World Soil Database v 1.2, FAO and IIASA [data set], available at https://webarchive.iiasa.ac.at/Research/LUC/External-World-soil-database/HTML/, last access 2/28/2022, 2012.

Feenstra, R. C., Inklaar, R., Timmer, M., and Woltjer, P.: Penn World Table 10.0, University of
1300   Groningen [data set], https://doi.org/10.15141/S5Q94M, 2015.

Feldmann, M., Emanuel, K., Zhu, L., and Lohmann, U.: Estimation of Atlantic Tropical Cyclone Rainfall Frequency in the United States, J. Appl. Meteorol. Climatol., 58, 1853–1866, https://doi.org/10.1175/JAMC-D-19-0011.1, 2019.

1305   Fiddes, J. and Gruber, S.: TopoSCALE v.1.0: downscaling gridded climate data in complex terrain, Geosci. Model Dev., 7, 387–405, https://doi.org/10.5194/gmd-7-387-2014, 2014.

Frieler, K., Volkholz, J., Lange, S., Schewe, J., Mengel, M., Otto, C., Jones, C., Reyer, C.P.O., Treu, S., Menz, C., Blanchard, J.L., Harrison, C.S., Petrik, C.M., Eddy, T.D., Ortega-Cisneros, K., Novaglio, C., Stock, C., Liu, X., Heneghan, R., Tittensor, D., Maury, O., Büchner, M., Vogt, T., Sauer, I., Koch, J., Lee, C.-Y., Carmago, S.J., Vanderkelen, I., Jägermeyr, J., Klar, J., Vega del Valle, I.D., Lasslop,
1310   G., Chadburn, S., Burke, E., Gallego-Sala, A., Smith, N., Chang, J., Hantson, S., Burton, C., Gädeke, A., Li, F., Gosling, S.N., Müller Schmied, H., Hattermann, F., Hickler, T., Marcé, R., Pierson, D., Thiery, W., Mercado-Bettín, D., Forrest, M., Bechtold, M., Kaplan, J.O., Koch, A.: Scenario Set-up and the new CMIP6-based climate-related forcings provided within the third round of the Inter-Sectoral Model Intercomparison Project (ISIMIP3b, group I and II), Geoscientific Model Development,
1315   submitted 2023.

Frieler, K., Lange, S., Piontek, F., Reyer, C. P. O., Schewe, J., Warszawski, L., Zhao, F., Chini, L., Denvil, S., Emanuel, K., Geiger, T., Halladay, K., Hurtt, G., Mengel, M., Murakami, D., Ostberg, S., Popp, A., Riva, R., Stevanovic, M., Suzuki, T., Volkholz, J., Burke, E., Ciais, P., Ebi, K., Eddy, T. D., Elliott, J., Galbraith, E., Gosling, S. N., Hattermann, F., Hickler, T., Hinkel, J., Hof, C., Huber, V.,
1320   Jägermeyr, J., Krysanova, V., Marcé, R., Müller Schmied, H., Mouratiadou, I., Pierson, D., Tittensor, D. P., Vautard, R., van Vliet, M., Biber, M. F., Betts, R. A., Bodirsky, B. L., Deryng, D., Frolking, S., Jones, C. D., Lotze, H. K., Lotze-Campen, H., Sahajpal, R., Thonicke, K., Tian, H., and Yamagata, Y.: Assessing the impacts of 1.5 °C global warming – simulation protocol of the Inter-Sectoral Impact Model Intercomparison Project (ISIMIP2b), Geosci. Model Dev., 10, 4321–4345,
1325   https://doi.org/10.5194/gmd-10-4321-2017, 2017.

Geiger, T., Frieler, K., and Bresch, D. N.: A global historical data set of tropical cyclone exposure (TCE-DAT), Earth System Science Data, 10, 185–194, https://doi.org/10.5194/essd-10-185-2018, 2018.

Golub, M., Thiery, W., Marcé, R., Pierson, D., Vanderkelen, I., Mercado-Bettin, D., Woolway, R. I.,
1330   Grant, L., Jennings, E., Kraemer, B. M., Schewe, J., Zhao, F., Frieler, K., Mengel, M., Bogomolov, V. Y., Bouffard, D., Côté, M., Couture, R.-M., Debolskiy, A. V., Droppers, B., Gal, G., Guo, M., Janssen, A. B. G., Kirillin, G., Ladwig, R., Magee, M., Moore, T., Perroud, M., Piccolroaz, S., Raaman Vinnaa, L., Schmid, M., Shatwell, T., Stepanenko, V. M., Tan, Z., Woodward, B., Yao, H., Adrian, R., Allan, M., Anneville, O., Arvola, L., Atkins, K., Boegman, L., Carey, C., Christianson, K., de Eyto, E., DeGasperi,
1335   C., Grechushnikova, M., Hejzlar, J., Joehnk, K., Jones, I. D., Laas, A., Mackay, E. B., Mammarella, I., Markensten, H., McBride, C., Özkundakci, D., Potes, M., Rinke, K., Robertson, D., Rusak, J. A., Salgado, R., van der Linden, L., Verburg, P., Wain, D., Ward, N. K., Wollrab, S., and Zdorovennova, G.: A framework for ensemble modelling of climate change impacts on lakes worldwide: the ISIMIP Lake Sector, Geosci. Model Dev., 15, 4597–4623, https://doi.org/10.5194/gmd-15-4597-2022, 2022.

1340   Gori, A., Lin, N., and Smith, J.: Assessing compound flooding from landfalling tropical cyclones on the North Carolina coast, Water Resour. Res., 56, https://doi.org/10.1029/2019wr026788, 2020.

Gori, A., Lin, N., Xi, D., and Emanuel, K.: Tropical cyclone climatology change greatly exacerbates US extreme rainfall–surge hazard, Nat. Clim. Chang., 12, 171–178, https://doi.org/10.1038/s41558-021-01272-7, 2022.

1345   Hersbach, H., Bell, B., Berrisford, P., Hirahara, S., Horányi, A., Muñoz-Sabater, J., Nicolas, J., Peubey, C., Radu, R., Schepers, D., Simmons, A., Soci, C., Abdalla, S., Abellan, X., Balsamo, G., Bechtold, P., Biavati, G., Bidlot, J., Bonavita, M., Chiara, G., Dahlgren, P., Dee, D., Diamantakis, M., Dragani, R., Flemming, J., Forbes, R., Fuentes, M., Geer, A., Haimberger, L., Healy, S., Hogan, R. J., Hólm, E., Janisková, M., Keeley, S., Laloyaux, P., Lopez, P., Lupu, C., Radnoti, G., Rosnay, P.,
1350   Rozum, I., Vamborg, F., Villaume, S., and Jean-Noël Thépaut: The ERA5 global reanalysis, Quart. J. Roy. Meteor. Soc., 146, 1999–2049, https://doi.org/10.1002/qj.3803, 2020.

Holland, G.: A Revised Hurricane Pressure–Wind Model, Mon. Weather Rev., 136, 3432–3445, https://doi.org/10.1175/2008MWR2395.1, 2008.

Holland, G. J.: An Analytic Model of the Wind and Pressure Profiles in Hurricanes, Mon. Weather Rev., 108, 1212–1218, https://doi.org/10.1175/1520-0493(1980)108<1212:AAMOTW>2.0.CO;2, 1980.

van den Hurk, B., Kim, H., Krinner, G., Seneviratne, S. I., Derksen, C., Oki, T., Douville, H., Colin, J., Ducharne, A., Cheruy, F., Viovy, N., Puma, M. J., Wada, Y., Li, W., Jia, B., Alessandri, A., Lawrence, D. M., Weedon, G. P., Ellis, R., Hagemann, S., Mao, J., Flanner, M. G., Zampieri, M., Materia, S., Law, R. M., and Sheffield, J.: LS3MIP (v1.0) contribution to CMIP6: the Land Surface, Snow and Soil moisture Model Intercomparison Project – aims, setup and expected outcome, Geosci. Model Dev., 9, 2809–2832, https://doi.org/10.5194/gmd-9-2809-2016, 2016.

Hurtt, G. C., Chini, L. P., Frolking, S., Betts, R. A., Feddema, J., Fischer, G., Fisk, J. P., Hibbard, K., Houghton, R. A., Janetos, A., Jones, C. D., Kindermann, G., Kinoshita, T., Klein Goldewijk, K., Riahi, K., Shevliakova, E., Smith, S., Stehfest, E., Thomson, A., Thornton, P., van Vuuren, D. P., and Wang, Y. P.: Harmonization of land-use scenarios for the period 1500–2100: 600 years of global gridded annual land-use transitions, wood harvest, and resulting secondary lands, Clim. Change, 109, 117, https://doi.org/10.1007/s10584-011-0153-2, 2011.

Hurtt, G. C., Chini, L., Sahajpal, R., Frolking, S., Bodirsky, B. L., Calvin, K., Doelman, J. C., Fisk, J., Fujimori, S., Klein Goldewijk, K., Hasegawa, T., Havlik, P., Heinimann, A., Humpenöder, F., Jungclaus, J., Kaplan, J. O., Kennedy, J., Krisztin, T., Lawrence, D., Lawrence, P., Ma, L., Mertz, O., Pongratz, J., Popp, A., Poulter, B., Riahi, K., Shevliakova, E., Stehfest, E., Thornton, P., Tubiello, F. N., van Vuuren, D. P., and Zhang, X.: Harmonization of global land use change and management for the period 850–2100 (LUH2) for CMIP6, Geosci. Model Dev., 13, 5425–5464, https://doi.org/10.5194/gmd-13-5425-2020, 2020.

IFASTAT: Statistics, International Fertilizer Association, IFASTAT Database [data set], available at: https://www.ifastat.org, last access: 21 January 2015.

ISIMIP Coordination Team, Sectoral Coordinators, Scientific Advisory Board: The Inter-Sectoral Impact Model Intercomparison Project (ISIMIP), Mission & Implementation Document, https://www.isimip.org/documents/646/MissionAndImplementation_12Sep2018_5Hlvj2N.pdf, 2018.

ISIMIP organigram: https://www.isimip.org/about/#organisational-structure, last access: 7 March, 2023

ISIMIP terms of use: https://www.isimip.org/gettingstarted/terms-of-use/, last access: 14 January 2023, 2022.

ISIMIP3a simulation protocol: https://protocol.isimip.org/#ISIMIP3a, last access: 14 January 2023.

Jägermeyr, J. and Frieler, K.: Spatial variations in crop growing seasons pivotal to reproduce global fluctuations in maize and wheat yields, Sci Adv, 4, eaat4517, https://doi.org/10.1126/sciadv.aat4517, 2018.

Jägermeyr, J., Müller, C., Ruane, A. C., Elliott, J., Balkovic, J., Castillo, O., Faye, B., Foster, I., Folberth, C., Franke, J. A., Fuchs, K., Guarin, J. R., Heinke, J., Hoogenboom, G., Iizumi, T., Jain, A. K., Kelly, D., Khabarov, N., Lange, S., Lin, T.-S., Liu, W., Mialyk, O., Minoli, S., Moyer, E. J., Okada, M., Phillips, M., Porter, C., Rabin, S. S., Scheer, C., Schneider, J. M., Schyns, J. F., Skalsky, R., Smerald, A., Stella, T., Stephens, H., Webber, H., Zabel, F., and Rosenzweig, C.: Climate impacts on global agriculture emerge earlier in new generation of climate and crop models, Nature Food, 2, 873–885, https://doi.org/10.1038/s43016-021-00400-y, 2021a.

Jägermeyr, J., Müller, C., Minoli, S., Ray, D., and Siebert, S.: GGCMI Phase 3 crop calendar, Zenodo [data set], https://doi.org/10.5281/ZENODO.5062513, 2021b.

Karger, D. N., Conrad, O., Böhner, J., Kawohl, T., Kreft, H., Soria-Auza, R. W., Zimmermann, N. E.,

Linder, H. P., and Kessler, M.: Climatologies at high resolution for the earth's land surface areas, Sci
Data, 4, 170122, https://doi.org/10.1038/sdata.2017.122, 2017.

Karger, D. N., Wilson, A. M., Mahony, C., Zimmermann, N. E., and Jetz, W.: Global daily 1 km land
surface precipitation based on cloud cover-informed downscaling, Sci Data, 8, 307,
https://doi.org/10.1038/s41597-021-01084-6, 2021.

Karger, D. N., Lange, S., Hari, C., Reyer, C. P. O., Conrad, O., Zimmermann, N. E., and Frieler, K.:
CHELSA-W5E5: Daily 1 km meteorological forcing data for climate impact studies, Earth System
Science Data Discussions [preprint], https://doi.org/10.5194/essd-2022-367, 2022a.

Karger, D. N., Lange, S., Hari, C., Reyer, C. P. O., and Zimmermann, N. E.: CHELSA-W5E5 v1.0:
W5E5 v1.0 downscaled with CHELSA v2.0, ISIMIP Repository [data set],
https://doi.org/10.48364/ISIMIP.836809.3, 2022b.

Khazaei, B., Read, L. K., Casali, M., Sampson, K. M., and Yates, D. N.: GLOBathy, the global lakes
bathymetry dataset, Sci. Data, 9, 36, https://doi.org/10.1038/s41597-022-01132-9, 2022.

Kim, H.: Global Soil Wetness Project Phase 3 Atmospheric Boundary Conditions (Experiment 1),
https://doi.org/10.20783/DIAS.501, 2017.

Klein Goldewijk, K.: HYDE 3.3, private communication, 2022.

Klein Goldewijk, K., Beusen, A., Doelman, J., and Stehfest, E.: Anthropogenic land use estimates for
the Holocene – HYDE 3.2, Earth Syst. Sci. Data, 9, 927–953, https://doi.org/10.5194/essd-9-927-
2017, 2017.

Knapp, K. R. and Kruk, M. C.: Quantifying Interagency Differences in Tropical Cyclone Best-Track
Wind Speed Estimates, Mon. Weather Rev., 138, 1459–1473,
https://doi.org/10.1175/2009MWR3123.1, 2010.

Knapp, K. R., Kruk, M. C., Levinson, D. H., Diamond, H. J., and Neumann, C. J.: The International
Best Track Archive for Climate Stewardship (IBTrACS): Unifying Tropical Cyclone Data, Bull. Am.
Meteorol. Soc., 91, 363–376, https://doi.org/10.1175/2009BAMS2755.1, 2010.

Koch, J. and Leimbach, M.: SSP economic growth projections: Major changes of key drivers in
integrated assessment modelling, Ecol. Econ., 206, 107751,
https://doi.org/10.1016/j.ecolecon.2023.107751, 2023.

Konzelmann, T., van de Wal, R. S. W., Greuell, W., Bintanja, R., Henneken, E. A. C., and Abe-Ouchi,
A.: Parameterization of global and longwave incoming radiation for the Greenland Ice Sheet, Glob.
Planet. Change, 9, 143–164, https://doi.org/10.1016/0921-8181(94)90013-2, 1994.

Krien, Y., Dudon, B., Roger, J., Arnaud, G., and Zahibo, N.: Assessing storm surge hazard and impact
of sea level rise in the Lesser Antilles case study of Martinique, Nat. Hazards Earth Syst. Sci., 17,
1559–1571, https://doi.org/10.5194/nhess-17-1559-2017, 2017.

Lange, S.: Trend-preserving bias adjustment and statistical downscaling with ISIMIP3BASD (v1.0),
Geosci. Model Dev., 12, 3055–3070, https://doi.org/10.5194/gmd-12-3055-2019, 2019.

Lange, S.: ISIMIP3BASD, Zenodo [data set], https://doi.org/10.5281/zenodo.4686991, 2021.

Lange, S. and Büchner, M.: ISIMIP3 land-sea masks, ISIMIP Repository [data set],
https://doi.org/10.48364/ISIMIP.822294, 2020.

Lange, S., Menz, C., Gleixner, S., Cucchi, M., Weedon, G. P., Amici, A., Bellouin, N., Schmied, H. M.,
Hersbach, H., Buontempo, C., and Cagnazzo, C.: WFDE5 over land merged with ERA5 over the
ocean (W5E5 v2.0), ISIMIP Repository [data set], https://doi.org/10.48364/ISIMIP.342217, 2021.

Lan, X., Tans, P., and Thoning, K. W.: Trends in globally-averaged CO2 determined from NOAA Global Monitoring Laboratory measurements, Version 2023-01 NOAA/GML, Global Monitoring Laboratory [data set], available at: https://gml.noaa.gov/ccgg/trends, 2023.

1445   Large, W. G. and Yeager, S. G.: The global climatology of an interannually varying air–sea flux data set, Clim. Dyn., 33, 341–364, https://doi.org/10.1007/s00382-008-0441-3, 2009.

Lee, M., Shevliakova, E., Stock, C. A., Malyshev, S., and Milly, P. C. D.: Prominence of the tropics in the recent rise of global nitrogen pollution, Nat. Commun., 10, 1437, https://doi.org/10.1038/s41467-019-09468-4, 2019.

Lehner, B., Reidy Liermann, C., Revenga, C., Vorosmarty, C., Fekete, B., Crouzet, P., Doll, P.,
1450   Endejan, M., Frenken, K., Magome, J., Nilsson, C., Robertson, J. C., Rodel, R., and Sindorf, N.: Global Reservoir and Dam Database, Version 1 (GRanDv1): Dams, Revision 01, NASA Socioeconomic Data and Applications Center [data set], https://doi.org/10.7927/H4N877QK, 2011a.

Lehner, B., Liermann, C. R., Revenga, C., Vörösmarty, C., Fekete, B., Crouzet, P., Döll, P., Endejan,
M., Frenken, K., Magome, J., Nilsson, C., Robertson, J. C., Rödel, R., Sindorf, N., and Wisser, D.:
1455   High-resolution mapping of the world's reservoirs and dams for sustainable river-flow management, Front. Ecol. Environ., 9, 494–502, https://doi.org/10.1890/100125, 2011b.

Lejeune, Q., Maskell, G., Menke, I., and Pleeck, S.: Stakeholder Survey Report, ISIMIP, available at: https://www.isimip.org/documents/376/ISIpedia_survey_result_report_w47NU6L.pdf, 2018.

Liu, X., Stock, C. A., Dunne, J. P., Lee, M., Shevliakova, E., Malyshev, S., and Milly, P. C. D.:
1460   Simulated global coastal ecosystem responses to a half-century increase in river nitrogen loads, Geophys. Res. Lett., 48, https://doi.org/10.1029/2021gl094367, 2021.

Loisel, J., Gallego-Sala, A. V., Amesbury, M. J., Magnan, G., Anshari, G., Beilman, D. W., Benavides, J. C., Blewett, J., Camill, P., Charman, D. J., Chawchai, S., Hedgpeth, A., Kleinen, T., Korhola, A., Large, D., Mansilla, C. A., Müller, J., van Bellen, S., West, J. B., Yu, Z., Bubier, J. L., Garneau, M.,
1465   Moore, T., Sannel, A. B. K., Page, S., Väliranta, M., Bechtold, M., Brovkin, V., Cole, L. E. S., Chanton, J. P., Christensen, T. R., Davies, M. A., De Vleeschouwer, F., Finkelstein, S. A., Frolking, S., Gałka, M., Gandois, L., Girkin, N., Harris, L. I., Heinemeyer, A., Hoyt, A. M., Jones, M. C., Joos, F., Juutinen, S., Kaiser, K., Lacourse, T., Lamentowicz, M., Larmola, T., Leifeld, J., Lohila, A., Milner, A. M., Minkkinen, K., Moss, P., Naafs, B. D. A., Nichols, J., O'Donnell, J., Payne, R., Philben, M., Piilo, S.,
1470   Quillet, A., Ratnayake, A. S., Roland, T. P., Sjögersten, S., Sonnentag, O., Swindles, G. T., Swinnen, W., Talbot, J., Treat, C., Valach, A. C., and Wu, J.: Expert assessment of future vulnerability of the global peatland carbon sink, Nat. Clim. Chang., 11, 70–77, https://doi.org/10.1038/s41558-020-00944-0, 2020.

Lu, P., Lin, N., Emanuel, K., Chavas, D., and Smith, J.: Assessing Hurricane Rainfall Mechanisms
1475   Using a Physics-Based Model: Hurricanes Isabel (2003) and Irene (2011), J. Atmos. Sci., 75, 2337–2358, https://doi.org/10.1175/JAS-D-17-0264.1, 2018.

Marsooli, R., Lin, N., Emanuel, K., and Feng, K.: Climate change exacerbates hurricane flood hazards along US Atlantic and Gulf Coasts in spatially varying patterns, Nat. Commun., 10, 3785, https://doi.org/10.1038/s41467-019-11755-z, 2019.

1480   Marzeion, B., Cogley, J. G., Richter, K., and Parkes, D.: Glaciers. Attribution of global glacier mass loss to anthropogenic and natural causes, Science, 345, 919–921, https://doi.org/10.1126/science.1254702, 2014.

Meinshausen, M., Smith, S. J., Calvin, K., Daniel, J. S., Kainuma, M. L. T., Lamarque, J.-F., Matsumoto, K., Montzka, S. A., Raper, S. C. B., Riahi, K., Thomson, A., Velders, G. J. M., and van
1485   Vuuren, D. P. P.: The RCP greenhouse gas concentrations and their extensions from 1765 to 2300, Clim. Change, 109, 213, https://doi.org/10.1007/s10584-011-0156-z, 2011.

Meinshausen, M., Vogel, E., Nauels, A., Lorbacher, K., Meinshausen, N., Etheridge, D. M., Fraser, P. J., Montzka, S. A., Rayner, P. J., Trudinger, C. M., Krummel, P. B., Beyerle, U., Canadell, J. G.,

1490   Daniel, J. S., Enting, I. G., Law, R. M., Lunder, C. R., O'Doherty, S., Prinn, R. G., Reimann, S., Rubino, M., Velders, G. J. M., Vollmer, M. K., Wang, R. H. J., and Weiss, R.: Historical greenhouse gas concentrations for climate modelling (CMIP6), Geoscientific Model Development, 10, 2057–2116, https://doi.org/10.5194/gmd-10-2057-2017, 2017.

Mengel, M., Treu, S., Lange, S., and Frieler, K.: ATTRICI v1.1 – counterfactual climate for impact attribution, Geosci. Model Dev., 14, 5269–5284, https://doi.org/10.5194/gmd-14-5269-2021, 2021.

1495   Messager, M. L., Lehner, B., Grill, G., Nedeva, I., and Schmitt, O.: Estimating the volume and age of water stored in global lakes using a geo-statistical approach, Nat. Commun., 7, 13603, https://doi.org/10.1038/ncomms13603, 2016.

Monfreda, C., Ramankutty, N., and Foley, J. A.: Farming the planet: 2. Geographic distribution of crop areas, yields, physiological types, and net primary production in the year 2000, Global Biogeochem.
1500   Cycles, 22, https://doi.org/10.1029/2007gb002947, 2008.

Muis, S., Apecechea, M. I., Dullaart, J., de Lima Rego, J., Madsen, K. S., Su, J., Yan, K., and Verlaan, M.: A high-resolution global dataset of extreme sea levels, tides, and storm surges, including future projections, Front. Mar. Sci., 7, https://doi.org/10.3389/fmars.2020.00263, 2020.

Müller Schmied, H.: DDM30 river routing network for ISIMIP3, ISIMIP Repository [data set],
1505   https://doi.org/10.48364/ISIMIP.865475, 2022.

Nicholls, R. J., Lincke, D., Hinkel, J., Brown, S., Vafeidis, A. T., Meyssignac, B., Hanson, S. E., Merkens, J.-L., and Fang, J.: A global analysis of subsidence, relative sea-level change and coastal flood exposure, Nat. Clim. Chang., 11, 338–342, https://doi.org/10.1038/s41558-021-00993-z, 2021.

van Oldenborgh, G. J., van der Wiel, K., Sebastian, A., Singh, R., Arrighi, J., Otto, F., Haustein, K., Li,
1510   S., Vecchi, G., and Cullen, H.: Attribution of extreme rainfall from Hurricane Harvey, August 2017, Environ. Res. Lett., 12, 124009, https://doi.org/10.1088/1748-9326/aa9ef2, 2017.

Outcomes of the ISIMIP Strategy Group Meeting: https://www.isimip.org/news/outcome-isimip-strategy-group-meeting-2018/, last access: 14 January 2023, 2018.

O'Neill, B., van Aalst, M., Z., Z. I., Berrang Ford, L., Bhadwal, S., Buhaug, H., Diaz, D., Frieler, K.,
1515   Garschagen, M., Magnan, A., Midgley, G., Mirzabaev, A., Thomas, A., and Warren, R.: Climate Change 2022: Impacts, Adaptation and Vulnerability. Key Risks Across Sectors and Regions, in: Contribution of Working Group II to the Sixth Assessment Report of the Intergovernmental Panel on Climate Change, edited by: Pörtner, H.-O., Roberts, D. C., Tignor, M., Poloczanska, E. S., Mintenbeck, K., Alegría, A., Craig, M., Langsdorf, S., Löschke, S., Möller, V., Okem, A., and Rama,
1520   B., Cambridge University Press, Cambridge, UK and New York, NY, USA, 2411–2538, https://doi.org/10.1017/9781009325844.025, 2022.

Patricola, C. M. and Wehner, M. F.: Anthropogenic influences on major tropical cyclone events, Nature, 563, 339–346, https://doi.org/10.1038/s41586-018-0673-2, 2018.

Peduzzi, P., Chatenoux, B., Dao, H., De Bono, A., Herold, C., Kossin, J., Mouton, F., and Nordbeck,
1525   O.: Global trends in tropical cyclone risk, Nat. Clim. Chang., 2, 289–294, https://doi.org/10.1038/nclimate1410, 2012.

Portmann, F. T., Siebert, S., and Döll, P.: MIRCA2000-Global monthly irrigated and rainfed crop areas around the year 2000: A new high-resolution data set for agricultural and hydrological modeling, Global Biogeochem. Cycles, 24, https://doi.org/10.1029/2008gb003435, 2010.

1530   Reyer, C., Silveyra Gonzalez, R., Dolos, K., Hartig, F., Hauf, Y., Noack, M., Lasch-Born, P., Rötzer, T., Pretzsch, H., Meesenburg, H., Fleck, S., Wagner, M., Bolte, A., Sanders, T., Kolari, P., Mäkelä, A., Vesala, T., Mammarella, I., Pumpanen, J., Matteucci, G., Collalti, A., D'Andrea, E., Foltýnová, L., Krejza, J., Ibrom, A., Pilegaard, K., Loustau, D., Bonnefond, J.-M., Berbigier, P., Picart, D., Lafont, S., Dietze, M., Cameron, D., Vieno, M., Tian, H., Palacios-Orueta, A., Cicuendez, V., Recuero, L., Wiese,
1535   K., Büchner, M., Lange, S., Volkholz, J., Kim, H., Weedon, G., Sheffield, J., Vega del Valle, I.,

Suckow, F., Horemans, J., Martel, S., Bohn, F., Steinkamp, J., Chikalanov, A., Mahnken, M., Gutsch, M., Trotta, C., Babst, F., and Frieler, K.: The PROFOUND database for evaluating vegetation models and simulating climate impacts on European forests. V. 0.3, GFZ Data Services [data set], https://doi.org/10.5880/PIK.2020.006, 2020a.

1540   Reyer, C. P. O., Silveyra Gonzalez, R., Dolos, K., Hartig, F., Hauf, Y., Noack, M., Lasch-Born, P., Rötzer, T., Pretzsch, H., Meesenburg, H., Fleck, S., Wagner, M., Bolte, A., Sanders, T. G. M., Kolari, P., Mäkelä, A., Vesala, T., Mammarella, I., Pumpanen, J., Collalti, A., Trotta, C., Matteucci, G., D'Andrea, E., Foltýnová, L., Krejza, J., Ibrom, A., Pilegaard, K., Loustau, D., Bonnefond, J.-M., Berbigier, P., Picart, D., Lafont, S., Dietze, M., Cameron, D., Vieno, M., Tian, H., Palacios-Orueta, A.,
1545   Cicuendez, V., Recuero, L., Wiese, K., Büchner, M., Lange, S., Volkholz, J., Kim, H., Horemans, J. A., Bohn, F., Steinkamp, J., Chikalanov, A., Weedon, G. P., Sheffield, J., Babst, F., Vega del Valle, I., Suckow, F., Martel, S., Mahnken, M., Gutsch, M., and Frieler, K.: The PROFOUND Database for evaluating vegetation models and simulating climate impacts on European forests, Earth Syst. Sci. Data, 12, 1295–1320, https://doi.org/10.5194/essd-12-1295-2020, 2020b.

1550   Reyer, C. P. O., Schelhaas, M.-J., Mäkelä, A., Peltoniemi, M., Gutsch, M., Mahnken, M., Loustau, D., Martel, S., Merganič, J., Merganičová, K., Meesenburg, H., Rötzer, T., Heym, M., Collalti, A., D'Andrea, E., Matteucci, G., Ibrom, A., and Kvist Johannsen, V.: Current Site-specific management guidelines and schedules for the 9 PROFOUND forest sites of the regional forest sector in ISIMIP, Zenodo, https://doi.org/10.5281/zenodo.7622027, 2023.

1555   Risser, M. D. and Wehner, M. F.: Attributable human-induced changes in the likelihood and magnitude of the observed extreme precipitation during hurricane Harvey, Geophys. Res. Lett., 44, 12,457–12,464, https://doi.org/10.1002/2017gl075888, 2017.

Rousseau, Y., Blanchard, J., Novaglio, C., Pinnell, K., Tittensor, D., Watson, R., and Ye, Y.: A data base of mapped global fishing activity, 1950-2017, Scientific Data, submitted 2023.

1560   Rousseau, Y., Blanchard, J., Novaglio, C., Kirsty, P., Tittensor, D., Watson, R., and Ye, Y.: Global Fishing Effort, IMAS [data set], https://doi.org/10.25959/MNGY-0Q43, 2022.

Rust, H. W., Kruschke, T., Dobler, A., Fischer, M., and Ulbrich, U.: Discontinuous Daily Temperatures in the WATCH Forcing Datasets, J. Hydrometeorol., 16, 465–472, https://doi.org/10.1175/JHM-D-14-0123.1, 2015.

1565   Sarmiento, J. L. and Gruber, N.: Ocean Biogeochemical Dynamics, Geol. Mag., 144, 1034–1034, https://doi.org/10.1017/S0016756807003755, 2006.

Seitzinger, S., Harrison, J. A., Böhlke, J. K., Bouwman, A. F., Lowrance, R., Peterson, B., Tobias, C., and Van Drecht, G.: Denitrification across landscapes and waterscapes: a synthesis, Ecol. Appl., 16, 2064–2090, https://doi.org/10.1890/1051-0761(2006)016[2064:dalawa]2.0.co;2, 2006.

1570   Sherman, K.: Large Marine Ecosystems, in: Encyclopedia of Ocean Sciences, Elsevier, 709–723, https://doi.org/10.1016/b978-0-12-409548-9.11117-0, 2017.

Slivinski, L. C., Compo, G. P., Whitaker, J. S., Sardeshmukh, P. D., Giese, B. S., McColl, C., Allan, R., Yin, X., Vose, R., Titchner, H., Kennedy, J., Spencer, L. J., Ashcroft, L., Brönnimann, S., Brunet, M., Camuffo, D., Cornes, R., Cram, T. A., Crouthamel, R., Domínguez-Castro, F., Freeman, J. E., Gergis,
1575   J., Hawkins, E., Jones, P. D., Jourdain, S., Kaplan, A., Kubota, H., Blancq, F. L., Lee, T.-C., Lorrey, A., Luterbacher, J., Maugeri, M., Mock, C. J., Moore, G. W. K., Przybylak, R., Pudmenzky, C., Reason, C., Slonosky, V. C., Smith, C. A., Tinz, B., Trewin, B., Valente, M. A., Wang, X. L., Wilkinson, C., Wood, K., and Wyszyński, P.: Towards a more reliable historical reanalysis: Improvements for version 3 of the Twentieth Century Reanalysis system, Quart. J. Roy. Meteor. Soc., 145, 2876–2908,
1580   https://doi.org/10.1002/qj.3598, 2019.

Slivinski, L. C., Compo, G. P., Sardeshmukh, P. D., Whitaker, J. S., McColl, C., Allan, R. J., Brohan, P., Yin, X., Smith, C. A., Spencer, L. J., Vose, R. S., Rohrer, M., Conroy, R. P., Schuster, D. C., Kennedy, J. J., Ashcroft, L., Brönnimann, S., Brunet, M., Camuffo, D., Cornes, R., Cram, T. A., Domínguez-Castro, F., Freeman, J. E., Gergis, J., Hawkins, E., Jones, P. D., Kubota, H., Lee, T. C.,

1585   Lorrey, A. M., Luterbacher, J., Mock, C. J., Przybylak, R. K., Pudmenzky, C., Slonosky, V. C., Tinz, B., Trewin, B., Wang, X. L., Wilkinson, C., Wood, K., and Wyszyński, P.: An Evaluation of the Performance of the Twentieth Century Reanalysis Version 3, J. Clim., 34, 1417–1438, https://doi.org/10.1175/JCLI-D-20-0505.1, 2021.

Smil, V.: Enriching the Earth: Fritz Haber, Carl Bosch and the Transformation of World Food
1590   Production, MIT Press, ISBN: 9780262194495, 2001.

Stock, C. A., Dunne, J. P., and John, J. G.: Global-scale carbon and energy flows through the marine planktonic food web: An analysis with a coupled physical–biological model, Prog. Oceanogr., 120, 1–28, https://doi.org/10.1016/j.pocean.2013.07.001, 2014.

Technical University of Denmark (DTU): Global Wind Atlas 3.0, released in partnership with World
1595   Bank Group, utilising data provided by Vortex, using funding provided by Energy Sector Management Assistance Program (ESMAP) [data set], available at: https://globalwindatlas.info, 2023.

Tian, H., Yang, J., Lu, C., Xu, R., Canadell, J. G., Jackson, R. B., Arneth, A., Chang, J., Chen, G., Ciais, P., Gerber, S., Ito, A., Huang, Y., Joos, F., Lienert, S., Messina, P., Olin, S., Pan, S., Peng, C., Saikawa, E., Thompson, R. L., Vuichard, N., Winiwarter, W., Zaehle, S., Zhang, B., Zhang, K., and
1600   Zhu, Q.: The Global N2O Model Intercomparison Project, Bull. Am. Meteorol. Soc., 99, 1231–1251, https://doi.org/10.1175/BAMS-D-17-0212.1, 2018.

Tittensor, D. P., Eddy, T. D., Lotze, H. K., Galbraith, E. D., Cheung, W., Barange, M., Blanchard, J. L., Bopp, L., Bryndum-Buchholz, A., Büchner, M., Bulman, C., Carozza, D. A., Christensen, V., Coll, M., Dunne, J. P., Fernandes, J. A., Fulton, E. A., Hobday, A. J., Huber, V., Jennings, S., Jones, M.,
1605   Lehodey, P., Link, J. S., Mackinson, S., Maury, O., Niiranen, S., Oliveros-Ramos, R., Roy, T., Schewe, J., Shin, Y.-J., Silva, T., Stock, C. A., Steenbeek, J., Underwood, P. J., Volkholz, J., Watson, J. R., and Walker, N. D.: A protocol for the intercomparison of marine fishery and ecosystem models: Fish-MIP v1.0, Geoscientific Model Development, 11, 1421–1442, https://doi.org/10.5194/gmd-11-1421-2018, 2018.

1610   Treu, S., Muis, S., Dangendorf, S., Wahl, S., Heinicke, S., Frieler, K., and M., M.: Hourly coastal water levels with long-term trends for impact attribution: the HLT Dataset, Earth System Science Data, submitted 2023.

Tsujino, H., Urakawa, S., Nakano, H., Small, R. J., Kim, W. M., Yeager, S. G., Danabasoglu, G., Suzuki, T., Bamber, J. L., Bentsen, M., Böning, C. W., Bozec, A., Chassignet, E. P., Curchitser, E.,
1615   Boeira Dias, F., Durack, P. J., Griffies, S. M., Harada, Y., Ilicak, M., Josey, S. A., Kobayashi, C., Kobayashi, S., Komuro, Y., Large, W. G., Le Sommer, J., Marsland, S. J., Masina, S., Scheinert, M., Tomita, H., Valdivieso, M., and Yamazaki, D.: JRA-55 based surface dataset for driving ocean–sea-ice models (JRA55-do), Ocean Model., 130, 79–139, https://doi.org/10.1016/j.ocemod.2018.07.002, 2018.

1620   United Nations, Department of Economic and Social Affairs: Population Division (2019), World Population Prospects 2019, archive [data set], https://population.un.org/wpp/Download/Archive/Standard/, 2019.

del Valle, I. V., Reyer, C., and Perrette, M.: ISIMIP3a wood harvesting input data (v1.1), ISIMIP Repository [data set], https://doi.org/10.48364/ISIMIP.482888.1, 2022.

1625   Wada, Y., van Beek, L. P. H., Viviroli, D., Dürr, H. H., Weingartner, R., and Bierkens, M. F. P.: Global monthly water stress: 2. Water demand and severity of water stress, Water Resour. Res., 47, https://doi.org/10.1029/2010wr009792, 2011.

Wada, Y., Lo, M.-H., Yeh, P. J.-F., Reager, J. T., Famiglietti, J. S., Wu, R.-J., and Tseng, Y.-H.: Fate of water pumped from underground and contributions to sea-level rise, Nat. Clim. Chang., 6, 777–780,
1630   https://doi.org/10.1038/nclimate3001, 2016a.

Wada, Y., Flörke, M., Hanasaki, N., Eisner, S., Fischer, G., Tramberend, S., Satoh, Y., van Vliet, M. T. H., Yillia, P., Ringler, C., Burek, P., and Wiberg, D.: Modeling global water use for the 21st century:

the Water Futures and Solutions (WFaS) initiative and its approaches, Geoscientific Model Development, 9, 175–222, https://doi.org/10.5194/gmd-9-175-2016, 2016b.

1635   Wang, J., Walter, B. A., Yao, F., Song, C., Ding, M., Maroof, A. S., Zhu, J., Fan, C., McAlister, J. M., Sikder, S., Sheng, Y., Allen, G. H., Crétaux, J.-F., and Wada, Y.: GeoDAR: georeferenced global dams and reservoirs dataset for bridging attributes and geolocations, Earth Syst. Sci. Data, 14, 1869–1899, https://doi.org/10.5194/essd-14-1869-2022, 2022.

Wang, S.-Y. S., Zhao, L., Yoon, J.-H., Klotzbach, P., and Gillies, R. R.: Quantitative attribution of
1640   climate effects on Hurricane Harvey's extreme rainfall in Texas, Environ. Res. Lett., 13, 054014, https://doi.org/10.1088/1748-9326/aabb85, 2018.

Wang, T. and Sun, F.: Global gridded GDP data set consistent with the shared socioeconomic pathways, Sci Data, 9, 221, https://doi.org/10.1038/s41597-022-01300-x, 2022.

Watson, R.: Global Fisheries Landings V4.0, IMAS [data set],
1645   https://doi.org/10.25959/5C522CADBEA37, 2019.

Watson, R. A. and Tidd, A.: Mapping nearly a century and a half of global marine fishing: 1869–2015, Mar. Policy, 93, 171–177, https://doi.org/10.1016/j.marpol.2018.04.023, 2018.

Whitehouse, P. L.: Glacial isostatic adjustment modelling: historical perspectives, recent advances, and future directions, Earth Surf. Dyn., 6, 401–429, https://doi.org/10.5194/esurf-6-401-2018, 2018.

1650   World Bank: World development indicators, World Bank Publications, Washington D.C., ISBN: 9780821373989, 2008.

Wöppelmann, G. and Marcos, M.: Vertical land motion as a key to understanding sea level change and variability, Rev. Geophys., 54, 64–92, https://doi.org/10.1002/2015rg000502, 2016.

Xi, D., Lin, N., and Smith, J.: Evaluation of a Physics-Based Tropical Cyclone Rainfall Model for Risk
1655   Assessment, J. Hydrometeorol., 21, 2197–2218, https://doi.org/10.1175/JHM-D-20-0035.1, 2020.

Yang, J. and Tian, H.: ISIMIP3a N-deposition input data, ISIMIP Repository [data set], https://doi.org/10.48364/ISIMIP.759077.1, 2020.

Yang, J., Yan, F., and Chen, M.: Effects of sea level rise on storm surges in the south Yellow Sea: A case study of Typhoon Muifa (2011), Cont. Shelf Res., 215, 104346,
1660   https://doi.org/10.1016/j.csr.2021.104346, 2021.

Zhang, X., Davidson, E. A., Mauzerall, D. L., Searchinger, T. D., Dumas, P., and Shen, Y.: Managing nitrogen for sustainable development, Nature, 528, 51–59, https://doi.org/10.1038/nature15743, 2015.

Zhao, N., Liu, Y., Cao, G., Samson, E. L., and Zhang, J.: Forecasting China's GDP at the pixel level using nighttime lights time series and population images, GISci. Remote Sens., 54, 407–425,
1665   https://doi.org/10.1080/15481603.2016.1276705, 2017.

Zhu, L., Quiring, S. M., and Emanuel, K. A.: Estimating tropical cyclone precipitation risk in Texas, Geophys. Res. Lett., 40, 6225–6230, https://doi.org/10.1002/2013gl058284, 2013.